

The influence of emissivity on the thermo-rheological modeling of the channelized lava flows at Tolbachik volcano

Michael Ramsey, Magdalena Oryaëlle Chevrel, Diego Coppola, Andrew J.L. J.L. Harris

▶ **To cite this version:**

Michael Ramsey, Magdalena Oryaëlle Chevrel, Diego Coppola, Andrew J.L. J.L. Harris. The influence of emissivity on the thermo-rheological modeling of the channelized lava flows at Tolbachik volcano. Annals of Geophysics, 2019, 61 (Vol 61 (2018)), 10.4401/ag-8077 . hal-02150633

HAL Id: hal-02150633
https://sde.hal.science/hal-02150633

Submitted on 7 Jun 2019

HAL is a multi-disciplinary open access archive for the deposit and dissemination of scientific research documents, whether they are published or not. The documents may come from teaching and research institutions in France or abroad, or from public or private research centers.

L'archive ouverte pluridisciplinaire **HAL**, est destinée au dépôt et à la diffusion de documents scientifiques de niveau recherche, publiés ou non, émanant des établissements d'enseignement et de recherche français ou étrangers, des laboratoires publics ou privés.

ISTITUTO NAZIONALE DI GEOFISICA E VULCANOLOGIA

ACCEPTED ON ANNALS OF GEOPHYSICS, 61, 2018; Doi: 10.4401/ag-8077

The influence of emissivity on the thermo-rheological modeling of the channelized lava flows at Tolbachik volcano

Michael S. Ramsey1, Magdalena Oryaëlle Chevrel2, Diego Coppola3, Andrew J.L. Harris2

1 Department of Geology and Environmental Science, University of Pittsburgh, 4107 O'Hara Street, Pittsburgh, PA 15260-3332, USA 9
2 Laboratoire Magmas et Volcans, Université Clermont Auvergne - CNRS - IRD, OPGC, Campus Universitaire des table Cézeaux, 6 Avenue Blaise Pascal, 63178 Aubière Cedex, France
3 Universita' Degli Studi Di Torino, Dipartimento Di Scienze Della Terra, Via Valperga Caluso, 15 35 – 10125, Torino, Italy

The influence of emissivity on the thermo-rheological modeling of the channelized lava flows at Tolbachik volcano

Michael S. Ramsey[1], Magdalena Oryaëlle Chevrel[2], Diego Coppola[3], Andrew J.L. Harris[2]

[1] Department of Geology and Environmental Science, University of Pittsburgh, 4107 O'Hara Street, Pittsburgh, PA 15260-3332, USA

[2] Laboratoire Magmas et Volcans, Université Clermont Auvergne - CNRS - IRD, OPGC, Campus Universitaire des tableCézeaux, 6 Avenue Blaise Pascal, 63178 Aubière Cedex, France

[3] Universita' Degli Studi Di Torino, Dipartimento Di Scienze Della Terra, Via Valperga Caluso, 35 – 10125, Torino, Italy

Submitted: 27 December 2018
Reviewed: 15 February 2019
Revised: 27 March 2019

Submitted to: Annals of Geophysics Special Issue - 2017 Catania MeMoVolc Workshop

Pages: 44
Tables: 4
Figures: 13

Address correspondence to:
Michael Ramsey
Department of Geology and Environmental Science
University of Pittsburgh
4107 O'Hara Street
Pittsburgh, PA 15260

phone: 412-624-8772
fax: 412-624-3914
email: mramsey@pitt.edu

Abstract.

The application of thermo-rheological models to forecast active lava flow emplacement and quantify important eruptive parameters of older flows has become a more common over the last decade. With the modification and adaption of these models to modular computing languages, they are now easier, quicker, and are being incorporated into studies of both terrestrial and planetary volcanism. These models rely on certain assumptions and input parameters, some of which such as emissivity are not well understood for molten materials. Without a well-grounded knowledge of how this parameter governs radiant cooling, remote measurements of temperature and models such as FLOWGO that rely on these temperatures to track cooling with time will be in error. Here, we perform a detailed FLOWGO-based modeling study of lava flows emplaced at Tolbachik volcano during the 2012-2013 and the 1975-1976 eruptions. Specifically, we have modified the FLOWGO model to incorporate a two-component emissivity model linked to the fraction of molten lava and cooled crust. We focus first on the large Leningradskoye Flow emplaced at the start of the 2012 eruption, relying on data from numerous other orbital sensors including MODIS, ASTER and ALI to constrain some of the model input parameters. The two-component emissivity adaption produced better fits to the final flow length, directly related to the crust cover percentage. We then applied the constrained model to the large Cone II flow formed in 1975, for which no satellite-based data are available. Results revealed that a nearly identical model fit was achieved with initial effusion rate of 700 m^3/s or 1250 m^3/s. However, for the higher the effusion rate, a lower the crust cover is needed to fit the flow length and width. This represents the first study to implement two-component emissivity into thermo-rheological modeling of lava flows. The results show that this is an important factor for model accuracy and

68 critical for large, higher effusion rate flows as well as for our understanding of older flows on
69 Earth and other planets.
70
71 **Introduction.**
72 Basaltic volcanism is ubiquitous on Earth and the other inner solar system bodies. Over half
73 of the world's volcanoes consist largely of basaltic-dominated systems occurring at every
74 tectonic setting and on every continent [Walker, 2000]. The basaltic volcanic eruptions at
75 Tolbachik in Russia (2012-2013); Bardarbunga in Iceland (2014); Etna in Italy (2018); Piton de
76 la Fournaise on Reunion Island (2018) and Kilauea in Hawaii (2018) reinforce the recurring
77 hazard potential of basaltic activity. The 2018 activity at Kilauea formed a very large, stable
78 channel from the vent to the ocean entry and destroyed numerous homes and property before
79 coming to an end [HVO, 2018; Neal et al., 2018]. Until the Kilauea eruption, the 2012-2013
80 eruption of Tolbachik volcano was the most thermally intense flow-forming eruption in the past
81 50 years, producing ~2.5 times more emitted energy than that of a typical eruption at Etna [e.g.,
82 MODVOLC, 2013; Pieri et al., 1990]. Monitoring flow propagation direction, velocity and effusion
83 rate, therefore, are critical for the flow models that have evolved over time. Several of these are
84 focused on heat loss and down-flow topography to predict flow advance [e.g., Dragoni 1989;
85 Favalli et al 2005; Garel et al 2014]. In addition to topography, the dominant (internal) factors
86 controlling flow propagation are the discharge rate combined with cooling and increasing
87 viscosity [e.g., Walker 1973; Miyamoto and Papp 2004; Harris and Rowland 2009]. All of these
88 models, however, rely on surface temperature, a key source term parameter that is commonly
89 measured using satellite- or ground-based thermal infrared (TIR) instruments [e.g., Flynn and
90 Mouginis-Mark 1992; Wright and Flynn 2003; Donegan and Flynn 2004]. It is the cooling of the

flow's uppermost radiating glassy surface that is directly imaged by these TIR instruments. Understanding the emissive properties of this surface thus becomes critical for any measurement or model reliant upon accurate knowledge of the kinetic temperature [e.g., Lillesand and Kiefer 1987; Ball and Pinkerton 2006; Harris 2013].

Thermo-rheological models of basaltic lava flows show that their morphological and dynamic evolution are governed by the interaction between the hot viscous core and the outer crust [e.g., Kilburn, 1993; Miyamoto and Sasaki, 1997; Miyamoto and Crown, 2006]. These models were developed to examine flow evolution, heat loss, and ultimately their spreading rate, advance velocity, inundation area and flow front arrival time [Harris and Rowland, 2001; Keszthelyi et al., 2000; Vicari et al., 2007]. A lava flow initially dissipates most of its heat radiatively, and with time and distance, forms a cooler glassy surface that will thicken, increase in viscosity, and eventually become a brittle crust [Hon et al. 1994]. With a constant lava discharge rate, the increase in crust thickness and flow viscosity will eventually force a flow to stop (e.g., a cooling-limited flow) [Guest et al. 1987; Rhéty et al. 2017]. Continued effusion upstream can then produce flow inflation and/or new break-outs and flow directions [Peterson et al. 1994; Crown and Baloga 1999]. The magnitude of a flow's radiative cooling is related most strongly to the surface temperature and percentage of insulating crust [Flynn and Mouginis-Mark 1994], whereas the efficiency of that cooling is directly proportional to the emissivity of the hot fraction of the lava's surface [Holman 1992; Ramsey and Harris, 2013, 2016].

Emissivity is the unitless, wavelength-dependent fundamental property of a material and is sensitive to its composition, state and structure [e.g., Crisp et al. 1990; Kahle et al. 1995; Burgi et al. 2002] because it is directly related to the vibrational motion of the atomic bonds within the material (i.e., the petrology and structural state of the material). It is also influenced by the

114 micron-scale surface roughness [Ramsey and Fink, 1999], and to a lesser degree, the look angle
115 between the instrument and surface [Ball and Pinkerton 2006]. Infrared spectra acquired
116 remotely may be used to distinguish bulk wt. % SiO_2, the presence of volcanic glass and the
117 surface texture/vesicularity [e.g., Moxham 1971; Crisp et al. 1990; Ramsey et al., 2012].
118 Changes in material state (i.e., solid vs. molten vs. amorphous) or structure (i.e., composition)
119 dramatically affect this infrared property. If emissivity is equal to unity at all wavelengths, the
120 material is said to be a blackbody or perfect radiator.

121 The radiative temperatures of flows derived from thermal cameras or satellite instruments
122 rely explicitly on knowledge of the surface emissivity, which is typically assumed close to unity
123 [see review in Ramsey and Harris, 2013]. Past anecdotal or poorly-constrained field
124 measurements hinted at the fact that a melt's emissivity was lower than the cooled surface [e.g.,
125 Abtahi et al., 2002]. If true, then so too is the derived effective radiation temperature [Pieri et al,
126 1990]. An incorrect overestimate of emissivity will, therefore, overestimate the calculated
127 radiative heat loss [e.g., Harris and Rowland, 2001; Keszthelyi and Denlinger, 1996; Keszthelyi
128 and Self, 1998], which has a direct consequence on the cooling rate and the modeled final run-
129 out distance. Conversely, for multispectral TIR measurements, an incorrectly derived
130 temperature results in an emissivity spectrum that is distorted in shape and incorrect in
131 magnitude limiting accurate estimates of composition [Rose et al., 2014].

132 Here, we examine the effect of different emissivity values for the molten and crust fractions
133 on the final length of channelized flows. More specifically, we use visible and infrared satellite
134 data during the 2012-2013 eruption of Tolbachik, Kamchatka (Russia) to constrain certain
135 modeling parameters used by PyFLOWGO [Chevrel et al., 2018]. These satellite data provide
136 important knowledge of the time-averaged discharge rate (TADR), channel width, radiant

emission, and fraction of crust, all of which are used to refine the model results. We then use the constrained model to examine the large Cone II Flow that was emplaced in the same region 36 years earlier during the “The Great Tolbachik Fissure Eruption" (GTFE), which started on 6 Jul 1975 and ended on 10 Dec 1976 [Fedotov et al., 1991].

The Tolbachik eruptions.

The Tolbachik complex (55.83° N, 160.33° E) is located on the Kamchatka Peninsula, Russia and is comprised of two volcanoes: Plosky (“flat”) Tolbachik (PT) with an elevation of 3,085 m and Ostry (“sharp”) Tolbachik (OT) at 3,682 m. The westernmost OT is a peaked stratovolcano and the easternmost PT is a flat-topped shield volcano with a collapse caldera that formed during the GTFE eruption. To the south of these peaks lie ~875 km^2 of basalt flows, pyroclastic deposits, and a NNE alignment of cinder cones called Tolbachik Dol (TD) or “valley” [Fedotov et al., 1991]. The GTFE was Kamchatka's largest volumetric basaltic eruption in historic times. The axial portion of TD concentrates in a narrow (3 – 4 km) zone where ~ 80% of all the eruptive centers are located (Figure 1). This eruption created a 20 km long chain of new cinder cones and flows, with the largest (the Cone II Flow) emanating from the second cone of the northern vents in the crater chain [Fedotov et al., 1991]. This flow formed between 6 July and 10 Sept 1975, with its central channel later covered by a smaller and thinner flow emplaced between 11 and 15 Sept 1975. The ~ 5 km long Cone II flow is 50 – 60 m thick with well-developed 30-m-high levees and a central channel that disappears down-flow where it spreads over flatter topography. In this zone, dominant flow folds (15 – 20 m high) are present perpendicular to the flow direction. Also present are regions of elevated thermal output that persist today. The slow cooling of this thick,

voluminous unit produces surface temperatures in excess of 100° C, which have been measured in the cracks on the crests of the large flow folds [Wessels et al., 2005].

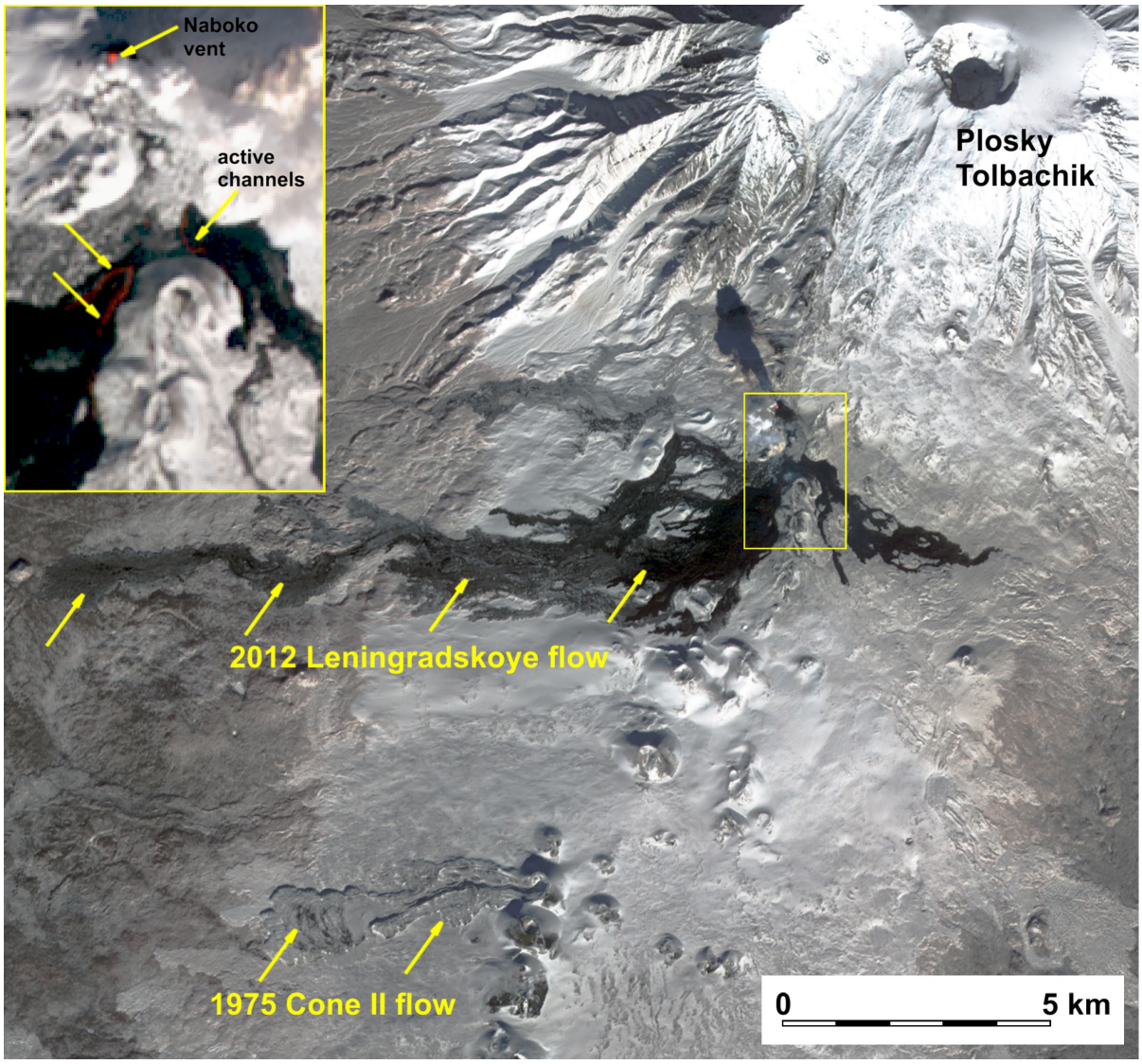


Figure 1. ASTER VNIR image acquired on 2 March 2013 centered on the Tolbachik Dol ("valley"), with channels 3 (0.807 μm), 2 (0.661 μm), 1 (0.556 μm) in red, green, blue, respectively. Spatial resolution is 15 m/pixel. The longest flow emplaced early in the eruption sequence is the Leningradskoye flow. Similarly, the other large flow analyzed here is the 1975 Cone II flow. Note the snow-free regions toward the flow's terminus due to elevated heat flow over 40 years after emplacement. Inset image is the TFE-50 vent region (brightened with a histogram equalization stretch) shown at full resolution. The active Naboko vent and channels shown in red are denoted by arrows.

After nearly four decades of quiescence, Tolbachik volcano began a new eruption in November 2012 that continued until September 2013. It is officially named the "'TFE-50 eruption"

173 after the 50th anniversary of the Institute of Volcanology and Seismology (IVS). Excellent details
174 on the chronology, style and character of the eruption and eruptive products are given by
175 Belousov et al. [2015] and Melnikov and Volynets [2015]. The Kamchatka Volcanic Eruption
176 Response Team (KVERT), which is part of IVS, initially reported episodes of volcanic tremor as
177 early as 7 Nov 2012 [BGVN, 2012]. That same day, observers from the village of Kozyrevsk (~
178 40 km W) reported ash explosions and a red glow seen in the same area as the northern vents
179 from the GTFE. Basaltic lava effused from two fissures along the west side of TD and a large
180 thermal anomaly was immediately detected in polar orbiting, low spatial resolution satellite data
181 [KVERT, 2012], which triggered later data acquisition from the high spatial resolution sensors
182 used in this study. Vigorous fire fountaining activity produced channel-fed, fast-moving lava flows
183 (Figure 2). By the time of the first cloud-free high spatial resolution orbital data acquisition by the
184 Advanced Land Imager (ALI) on 1 Dec 2012, the primary flow (later named the Leningradskoye
185 flow) emanating from the Naboko vent had already reached 11.3 km in length (Figure 3),
186 eventually growing to ~ 14 km on 3 Dec, and ~ 17 km by 8 Dec with numerous smaller breakouts
187 and new flows occurring over the subsequent months. The Leningradskoye flow is channelized,
188 15 m thick a'a flow [Belousov et al., 2015]. It advanced at ~200m/h fed by the high effusion rates
189 in the initial stage of the eruption. During this early phase of high effusion rates, the flow initially
190 traveled through a deep and narrow channel with a velocity of 2-3 m/s [Belousov et al., 2015].
191 The flow within the channel was relatively uncrusted, which changed several weeks later as the
192 discharge rate dropped and a short tube formed at the upper part of the channel near the vent.
193 Lava emerging from the tube at this point in time was nearly completely covered by a flexible,
194 frothy crust 5-10 cm thick [Belousov et al., 2015].
195



Figure 2. Aerial photographs of the Leningradskoye flow's open channel taken in the first week of the eruption. Image is looking east toward the fissure that intersected the Krasny cone (approximately 2km in the background). The channel is covered by ~ 40% cooler crust. Inset shows a photograph taken on the same day of the same channel ~ 2km downstream. Here, the channel is covered with ~ 70% crust. Photographs courtesy of the Institute of Volcanology and Seismology (IVS), FEB RAS, KVERT.

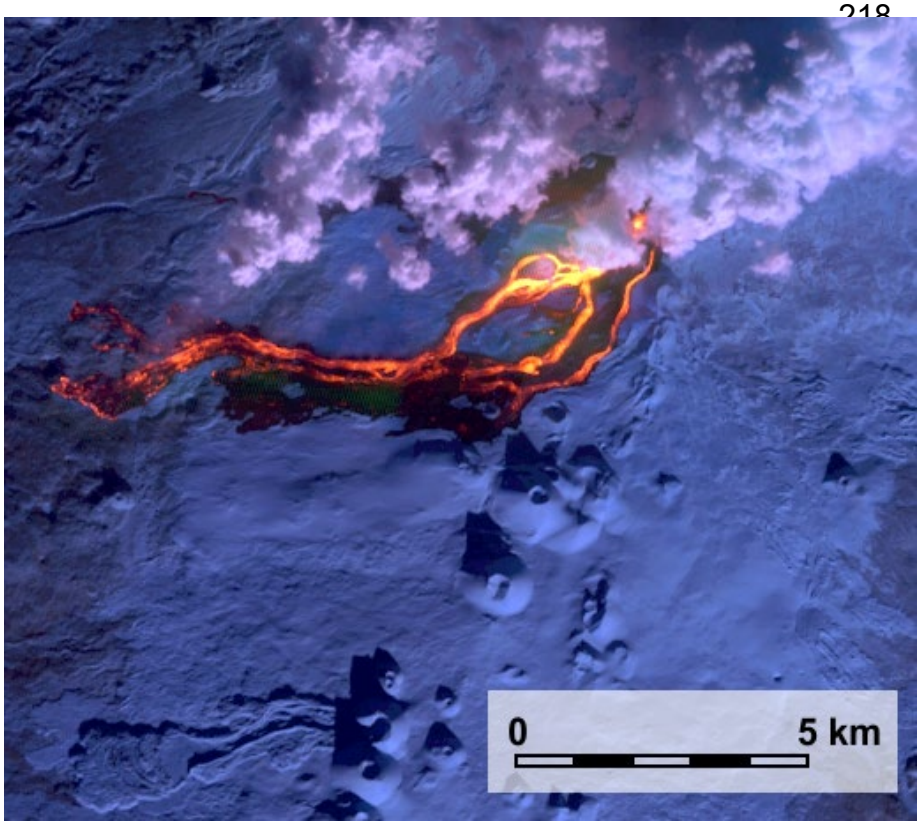


Figure 3. EO-1 ALI image of the Leningradskoye flow acquired on 1 Dec 2012 with channels 9 (1.65 μm), 8 (1.25 μm), 7 (0.87 μm) in red, green, blue, respectively. A square root stretch has been applied. Spatial resolution is 30 m/pixel. The increase color intensity in bands 8 and 9 (bright yellow) indicates the highest temperatures (open lava channels and the vent).

Lava effusion rates were calculated independently by several different methodologies. Aerial surveys on 29 Nov 2012 by IVS scientists reported an initial average effusion rate of 440 m^3/s decreasing to 140 m^3/s two weeks later [Gordeev et al., 2013; Dvigalo et al., 2014]. This compares to the time-averaged discharge rate (TADR) derived from Moderate Resolution Imaging Spectroradiometer (MODIS) data of 278 m^3/s on 1 Dec 2012, decreasing to an average of 102 m^3/s in the following two weeks (Figure 4). It should be noted that the TADR values can have up to 30% error and represent a discharge rate averaged over the 12-24 hours prior to the image acquisition [Coppola et al., 2010]. TADR were also calculated throughout the eruption following each cloud-free high resolution satellite image. Ramsey and Harris [2016] mapped the change in flow area using the high spatial resolution satellite data and a constant flow thickness of 5m (based on field reporting at the time) [e.g., Gordeev at al., 2013]. The volumes are reported in Table 1. Throughout 2013, the flow field expanded later being redirected to the eastern side of the vent chain, eventually building three flow fields (Vodopadnoye to the NW, Leningradskoye to the SW, and Toludskoye to the SE) that covered over 35 km^2 [Dvigalo et al., 2013].

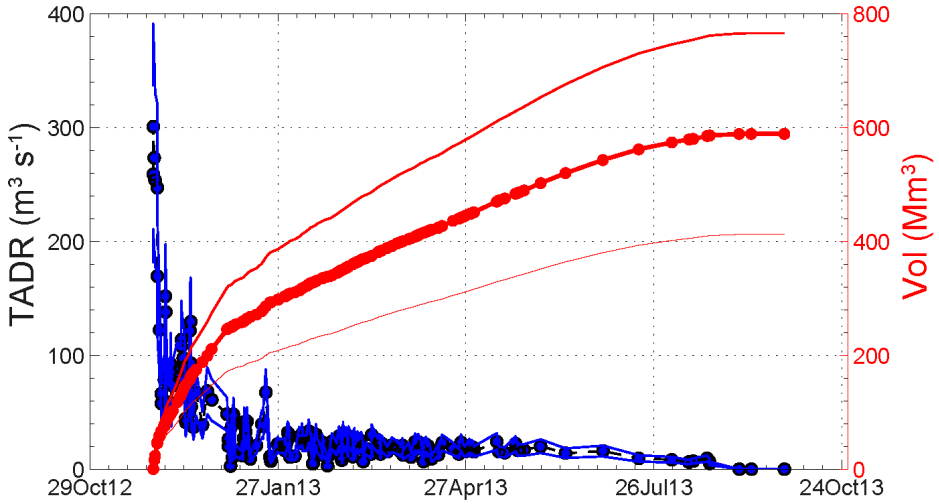


Figure 4. MIROVA time averaged discharge rate (TADR) plot (blue circles) calculated using eq. 3. Also shown is the cumulative volume of erupted lava (red circles). A standard error of ± 30% is shown by the thinner lines on both plots.

DATE	DAY	FLOW FIELD AREA (km^2)	EFFUSION RATE (m^3/s)
12/01/12	5	20.3	141
12/02/12	6	21.5	42
12/11/12	15	23.6	8
12/22/12	26	24.0	1
01/12/13	47	25.2	2

Table 1. Results of the first phase of the Tolbachik eruption using high spatial resolution satellite data to map flow field area and calculate effusion rate assuming a constant flow thickness of 5m. These results, calculated in real-time with each new satellite image acquired, compare quite well with later studies of the flow dimensions [Dvigalo et al., 2013; Gordeev et al., 2013].

Information on the erupted lava petrology is an important parameter constraint for the PyFLOWGO modeling. Petrologic information for the 1975 GTFE eruption comes from Fedotov et al. [1991] with the lava flow from Cone II falling into their “northern vents” category. These lavas are classified as magnesian basalt with moderate alkalinity, having a range of eruption temperature of 900 – 1050 °C. Field-based estimates of lava viscosity made from lava flow front velocities ranged widely from 10^4 – 10^{10} Pa·s [Vende-Kirkov, 1978; Fedotov et al. 1991]. One would expect a composition other than basalt for all but the very low end of this range, which was not the case. The northern vent lavas had an average bulk SiO_2 wt. % of ~ 50 and 20 vol. % phenocrysts, primarily clinopyroxene and olivine (3-8 mm). In contrast, Belousov et al. [2015] reported that the lavas from the 2012 TFE-50 eruption were more evolved with a slightly higher SiO_2 content of 52 – 53 wt. %. This, combined with the higher alkalinity, classifies these lavas as basaltic trachyandesites (Table 2). Over time, the erupted lavas became more basic with SiO_2 weight percentages decreasing. Plecheov et al. [2015] reports the average crystal content for the Naboko vent lavas, which produced the Leningradskoye flow, ranged from 23 – 29 vol. % with a porosity of ~ 6 vol. %. The primary crystals were plagioclase, olivine and titanomagnetite. Based on geothermometry analyses, they estimate the eruptive lava temperature was ~1080 °C.

OXIDE	2012 FLOW (wt. %)	1975 FLOW (wt. %)
SiO_2	51.75	50.50
TiO_2	1.94	0.89
Al_2O_3	16.31	13.88
FeO	8.38	7.09
Fe_2O_3	2.34	1.99
MnO	0.20	0.18
MgO	4.39	9.86
CaO	7.31	11.55
Na_2O	3.93	2.55
K_2O	2.40	0.79
P_2O_5	0.75	0.23
LOI (~H_2O)	0.30	0.47

Table 2. X-ray fluorescence analysis of major oxides done for this study, comparing one sample from the 1975 GTFE to one from the 2012 TFE-50 Tolbachik eruptions. The 2012 sample is higher in AlO_3 as reported by Gordeev et al. [2013] and Belousov et al. [2015], plotting in the same geochemical space as their sample analyses. Comparing the SiO_2 wt. % to the sum of the K_2O + NaO_2 wt. %, classifies the 1975 sample as a basalt and the 2012 sample as a basaltic trachyandesite, consistent with prior studies. Reported LOI is assumed equal to H_2O because of the basaltic rock composition.

Datasets and Modeling.

High spatial resolution satellite data

The Advanced Land Imager (ALI) was launched aboard the Earth Observing-1 (EO-1) spacecraft in November 2000, and was deactivated by NASA in 2017. ALI had ten spectral channels in the visible/short wave infrared (VSWIR) region (0.43 – 2.35 μm) with nine having a spatial resolution of 30 m and one (the panchromatic channel) spanning 0.48 – 0.69 μm with 10 m resolution. The data were collected in four swaths, which spanned 37 km in width, with each swath having a length that varied from 42-185 km [Digenis et al., 1998; Hearn et al., 2001]. ALI acquired numerous observations of the flows throughout the 2012-13 eruptive phase, including the first clear higher resolution image on 1 Dec 2012.

The Advanced Spaceborne Thermal Emission and Reflection Radiometer (ASTER) was launched on the Terra spacecraft in December 1999 and measures ground-leaving radiance in 14 spectral channels [Yamaguchi et al., 1998]. With the failure of the shortwave infrared (SWIR)

299 subsystem in 2009, only two subsystems remain, each with different spatial/spectral resolutions:
300 the visible/near infrared (VNIR) sensor with three channels (0.56–0.81 μm) at a 15 m spatial
301 resolution and the TIR sensor with five channels (8.2–11.3 μm) with 90 m spatial resolution.
302 ASTER was tasked to acquire data of the Tolbachik eruption at every observational opportunity
303 (both day and night) from early Dec 2012 until late June 2013 (Figure 5).

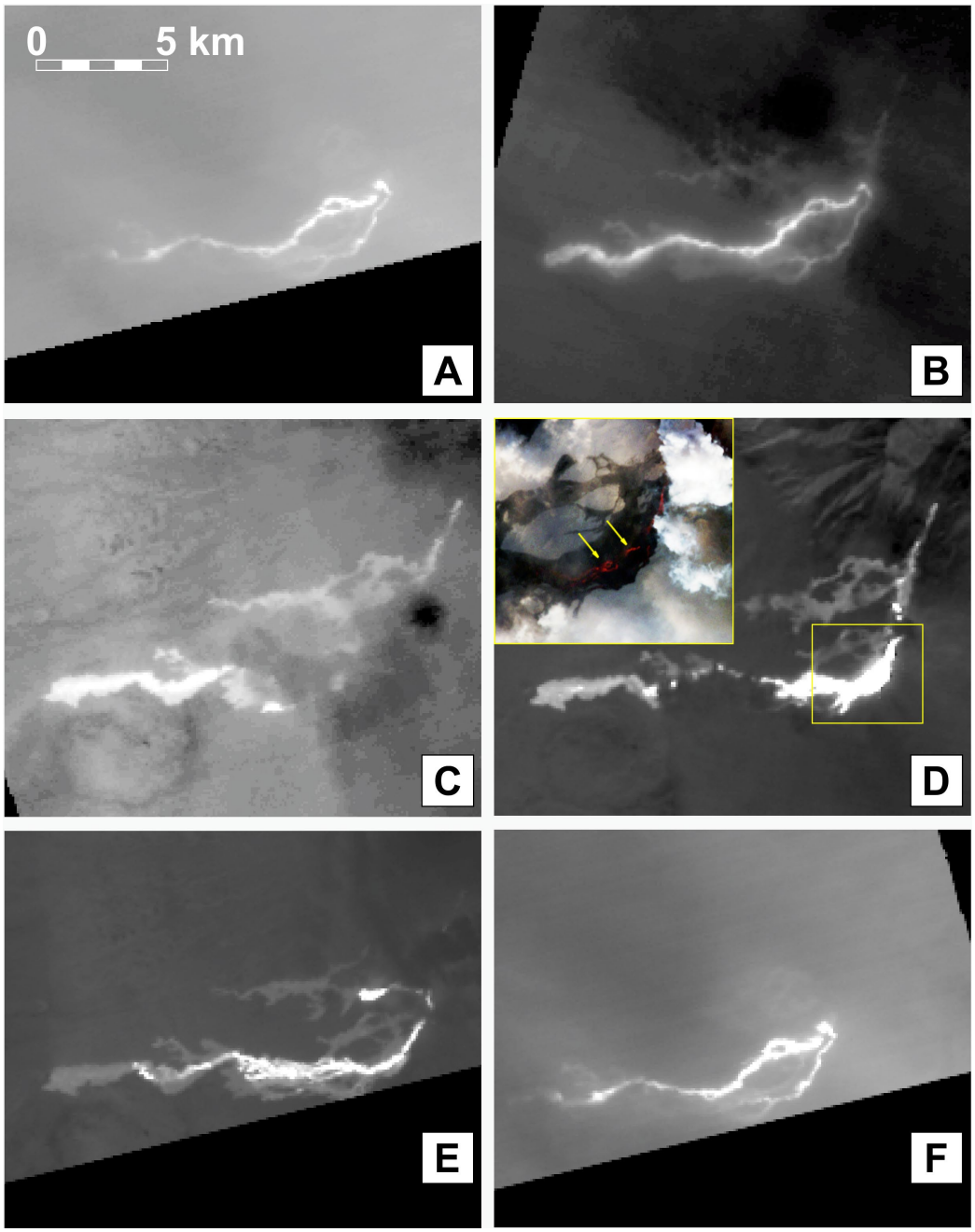


Figure 5. Time series of ASTER TIR data acquired over the first 3 weeks of the TFE-50 eruption. All images are shown at the same scale, with a guassian stretch applied. Spatial resolution is 90 m/pixel. The (n) or (d) after the date refers to data acquired at night or day local time, respectively. (A) 2 Dec 2012 (n). (B) 3 Dec 2012 (d). (C) 11 Dec 2012 (n). (D) 12 Dec 2012 (d). (E) 18 Dec 2012 (n). (F) 20 Dec 2012 (n). Images A – C and F contain various degrees of intervening cloud cover, though not enough to entirely block the TIR radiance, but significant enough to blur details and make accurate temperature retrievals impossible. Image D contains an inset of the VNIR data from the same date, which is able to resolve the individual open channels (shown by yellow arrows).

The ASTER science team also produced two versions of a global DEM (GDEM) dataset, which averages all the ASTER scenes acquired over a given region. This process greatly reduces instrument noise related errors and removes most cloud artifacts [Fujisada et al., 2005]. Version 1 (v1), released in 2009, was compiled from over 1.2 million individual scenes. The improved GDEM version 2 (v2) was released in 2011 adding 260,000 additional DEMs acquired from 2008 - 2011, improving coverage and further reducing data artifacts. The refined production algorithm for v2 also provides finer horizontal resolution and increased accuracy (e.g., vertical accuracy of ~17 m on average) [Tachikawa et al., 2011].

The ASTER GDEM v2 is used as the topographic base layer of choice for the analysis of the Cone II flow from the 1975-76 eruption. The creation of GDEM v2 ended with data acquired prior to the start of the TFE-50 eruption. Therefore, we rely on the single-scene DEM's for the 2012-13 eruption. Pre-flow topography is extracted by mapping the position of the 2012 flow channels from the ALI SWIR data and ASRER TIR data on the GDEM. These elevation data are used in PyFLOWGO (Figure 6). Individual ASTER scene DEMs collected during the eruption were analyzed to determine channel width, flow thickness, and channel topography where possible. However, the presence of volcanic fume and cloud combined with the scene-dependent noise limited the use of the individual scene DEMs. Pre-flow topography for the 1975 flow was extracting from the GDEM using transects next to the flow and directly down the centerline of the main channel. Channel widths of this larger flow are also easily resolved in the GDEM data. Five channel cross sections were extracted down the length of the flow and used to constrain PyFLOWGO model runs.

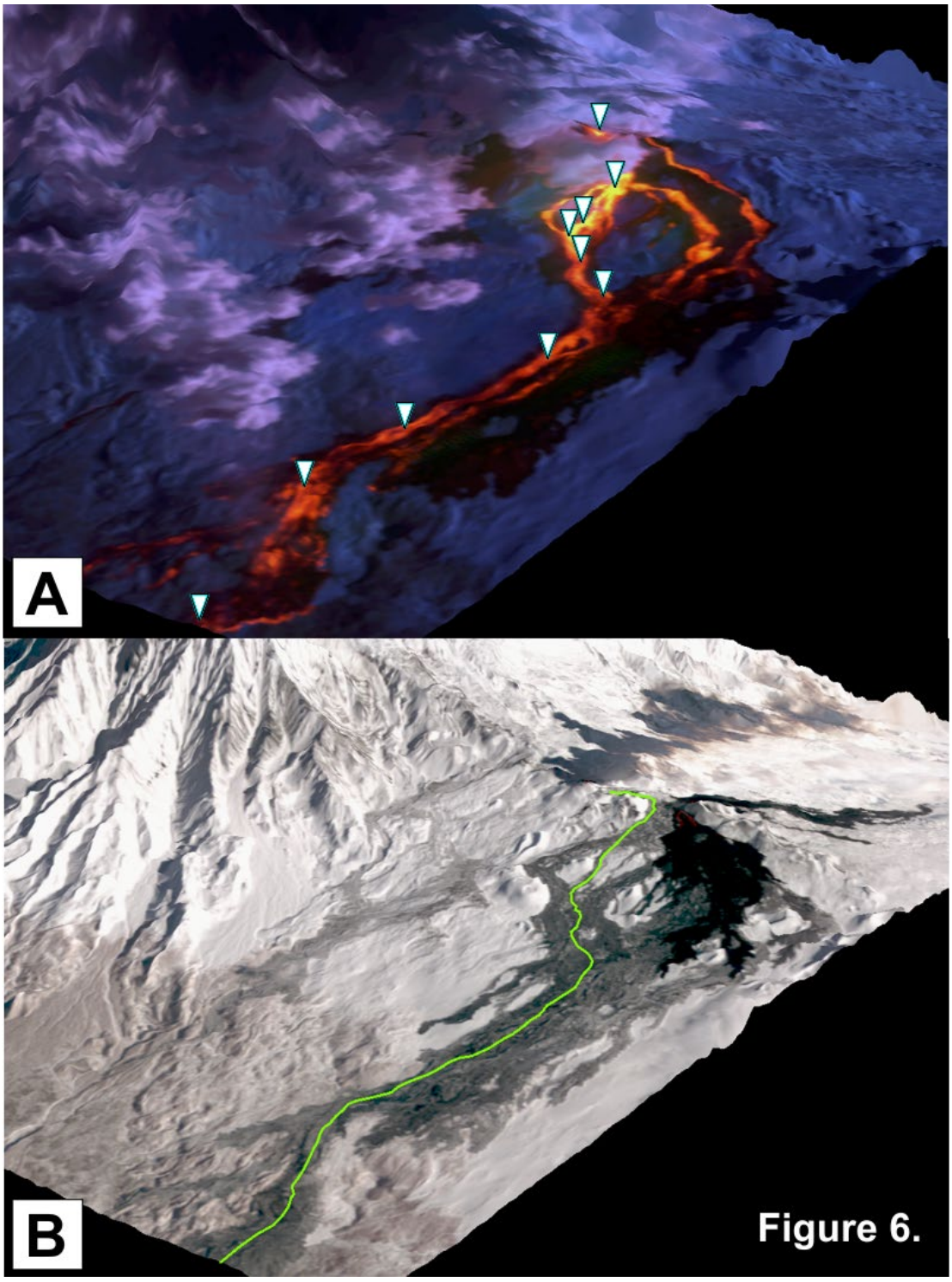


Figure 6. High resolution orbital data draped over the ASTER-derived DEM produced from the VNIR image acquired on 28 Feb 2013. DEM posting = 30 m. (A) ALI image acquired on 1 Dec 2012 with channels 9, 8, 7 in red, green, blue, respectively (see Figure 3). White triangles denote extracted radiance locations (see Figure 8B). (B) ASTER image acquired on 28 Feb 2013 with channels 3, 2, 1 in red, green, and blue, respectively. The active channel in the ALI image was traced, exported as a vector and shown in green.

High temporal resolution satellite data

The MODerate resolution Imaging Spectroradiometer (MODIS) is carried on both the Terra and Aqua NASA-EOS satellites, which have been flown in sun-synchronous polar orbits since February 2000 and May 2002, respectively. The two MODIS instruments provide radiometric data in 36 spectral bands from 0.4 μm to 14.4 μm. Of these, 29 channels collect data in the IR region with a nominal spatial resolution of 1 km at nadir. The ±55-degree scan angle produces 2330 km swath widths with data acquired approximately four times per day for a given target. At the higher latitudes of the Kamchatka peninsula, however, 6-10 overpasses per day are common due to pole-ward orbit convergence. MODIS IR channels, include a middle infrared (MIR) and a TIR channel, centered at 3.96 μm (channels 21 & 22), and 12.02 μm (channel 32), respectively. These are typically used to detect high-temperature volcanic thermal anomalies [Wright et al., 2002; Coppola et al., 2016].

MIROVA System

MIROVA (Middle Infrared Observation of Volcanic Activity) is an automated global hot spot detection system (http://www.mirovaweb.it) based on near-real time MODIS data [Coppola et al. 2016]. The system completes automatic detection and location of high-temperature thermal anomalies through a series of processing steps. The system provides a quantification of the Volcanic Radiative Power (VRP in Watts), by means of the MIR method of Wooster et al. [2003]:

$$VRP = 18.9 \cdot A_{pixel} \cdot \sum_{i=1}^{npix} R_{MIR,alert} - R_{MIR,bk} \quad \text{(eq. 1)}$$

where *npix* is the number of hot-spot contaminated pixels, A_{pixel} is the pixel size (1 km^2 for MODIS) and $R_{MIR,alert}$ and $R_{MIR,bk}$ are the pixel-integrated MIR radiances (at 3.96 μm) of the i^{th} alerted pixel(s) and background, respectively. According to Wooster et al. [2003], the constant

of proportionality (18.9 $m^2 \cdot \mu m \cdot sr$) in the equation allows estimations of VRP (± 30%) from hot surfaces having temperatures ranging from 600 - 1500 K. This makes the application of eq. 1 to the lava flow surface a practical way to estimate the radiant flux of the active portion of the flow field, with essentially no contribution from the cooler and cooling flow areas. The cumulative Volcanic Radiative Energy (VRE) in Joules is calculated as the trapezoidal integration of the VRP time series.

During effusive eruptions, the calculation of Time Averaged Discharge Rate (TADR) of lava using satellite thermal data is an important input parameter for later modelling lava flow advances and dynamics [Harris et al., 2016]. This approach, commonly referred to as the "thermal proxy", is derived from the contribution of several studies that have continuously revised and refined the theoretical framework and its practical application to real cases [e.g., Pieri and Baloga 1986; Crisp and Baloga 1990; Harris et al., 1998; Wright et al., 2001; Harris et al., 2007a; Harris and Baloga 2009; Dragoni and Tallarico 2009, Coppola et al, 2013; Garel et al., 2012, 2014, 2015, Tarquini et al., 2017]. A specific analysis of the TADR calculations using MODIS-MIROVA data [Coppola et al., this volume] outlines the methods and limits of this approach during the emplacement of large lava flows, such as the case for the TFE-50 Tolbachik eruption. Following Coppola et al. [2013], a single coefficient, called radiant density (c_{rad} in J m^{-3}), can be calculated to describe the appropriate relationship between radiated energy (VRE) and erupted volume (Vol) for the observed eruption:

$$c_{rad} = \frac{VRE}{Vol} \quad \text{(eq. 2)}$$

For the Tolbachik eruption we considered a total volume of the lava flow of ~573 x 10^6 m^3 [Dai and Howatt, 2017] and calculated a c_{rad} equal to 1.08 × 10^8 J m^{-3}, a value typical of lava

flows having mafic composition [Coppola et al., 2013]. It follows that for any VRP measurements, the corresponding TADR can be calculated following:

$$TADR = \frac{VRP}{c_{rad}} \quad \text{(eq. 3)}$$

Sensor webs

The improved temporal coverage of the Tolbachik TFE-50 eruption by the ALI and ASTER sensors was made possible by detection and communication protocols, as well as software to implement those protocols, all designed to create "sensor web" networks [Davies et al., 2016; Ramsey et al., 2016]. Both ASTER and ALI have 16-day nominal repeat observational frequencies at the equator, which improves at higher latitudes due to the convergence of overlapping orbit swaths. However, with the sensor web programs, these time periods are greatly improved [see Davies et al., 2016; Ramsey et al., 2016].

The sensors on the EO-1 spacecraft were used as part of the Volcano Sensor Web (VSW), which relied on onboard software for rapid scheduling and data processing using reports of volcanic unrest as triggers [Davies et al., 2016]. The VSW did not rely solely on detections from other orbital sensors, but also ground-based detection and communicated reports. The rapid retasking of the spacecraft, off-nadir pointing as well as the use of onboard data processing and downloading commonly enabled very rapid response times to volcanic eruptions.

A program that links high temporal/low spatial resolution data detection of thermally-elevated anomalies to specific scheduling of ASTER data has been in place since 2004 [Ramsey and Dehn, 2004; Carter et al., 2007, 2008; Rose and Ramsey, 2009; Duda et al., 2009; Ramsey, 2016]. The urgent request protocol (URP) global system started with (and has been heavily focused on) the northern Pacific region [Duda et al., 2009; Ramsey and Harris, 2013; Ramsey,

443 2015]. The URP program allows data acquisition frequency as high as night-day-night
444 observational triplets acquired approximately every two weeks and day-night pairs acquired
445 approximately every five days during the Tolbachik eruption.

446 The presence of the VSW and the URP provided a much larger volume of higher spatial
447 resolution data than would normally be available for such an eruption. For example, ALI acquired
448 the first high resolution image of the Tolbachik eruption on 1 Dec 2012, whereas the first clear
449 ASTER observation came ~ 30 hours later during a nighttime overpass. ASTER was also able
450 to acquire a daytime scene only 13.5 hours later due to the orbit configuration of the Terra
451 satellite [Ramsey, 2016]. During the first seven months of the Tolbachik eruption, there were 48
452 cloud free/nearly cloud free acquisitions by all high resolution satellite instruments (an average
453 of one scene approximately every 4 days). Of the total number of scenes, 33 were ASTER, 11
454 were ALI and 4 were from other sensors. The data acquired in the first few weeks of the eruption
455 in particular provided some of the best synoptic views, documenting vent locations, flow
456 lengths/direction, channel widths and their changes over time (Figure 5).

457

458 *PyFLOWGO modeling*

459 The original one-dimensional FLOWGO model tracks the thermal and rheological evolution
460 of a lava control volume using a series of heat loss equations coupled with the Jeffreys equation
461 for Newtonian flow in an open channel, modified for a Bingham fluid [Harris and Rowland, 2001;
462 Harris and Rowland, 2014]. Lava is tracked down-flow with its cooling, crystallization, viscosity
463 and yield strength re-calculated at each down-flow step to estimate the velocity [Harris et al.,
464 2007b; Riker et al., 2009; Robert et al., 2014]. The model was applied to various cooling limited
465 lava flows [Harris and Rowland, 2001, Harris et al., 2005, Harris and Rowland, 2012, Rhéty et

al., 2017]. PyFLOWGO [Chevrel et al. 2018] implements the model using the Python open source software [van Rossum, 1995].

To correctly simulate the evolution of down-flow lava properties, the user is allowed to change the input parameters as well as the thermo-rheological models (i.e. heat loss mechanisms, crystallization rate, temperature- and crystallinity-dependent viscosity, crust cover fraction, etc.) within plausible limits [e.g. Harris et al., 2007b] so as to best-fit a natural flow. Input parameters cover broad categories of channel dimension, eruption conditions, the radiative, conductive, convective parameters, and material properties of the lava. Within these categories are some terms (typically assumed) that are specifically related to (and derived from) the TIR radiance, including emissivity, lava/crust temperatures, and vesicularity. Typically, lava emissivity and vesicularity are assumed and held constant throughout a model run as the temperature of the crust cools. As originally specified by Harris and Rowland [2001], the fraction of this crust increases down-flow as flow velocity decreases (rather than being a function of the radiative cooling), implying a flow regime in which the crust is more stable at lower flow velocities (and presumably lower temperatures).

For thermo-rheological models such as PyFLOWGO that rely on radiant cooling, the question arises: to what degree does an incorrect emissivity (and perhaps other) assumption(s) affect the final model results. To first test whether emissivity plays a significant role in the radiant cooling, and therefore in determining the final cooling-limited flow length, we modified PyFLOWGO with a radiative heat flux (Q_{rad}) model that uses an "effective" emissivity:

$$Q_{rad} = \sigma \varepsilon_{eff} T_{eff}^4 \qquad \text{(eq. 4)}$$

Here, it is not just the effective radiation temperature (T_{eff}) that depends on the crustal fraction (f_{crust}), but also the effective emissivity (ε_{eff}). This allows the effective emissivity to be computed

via a *two-component emissivity model* where the cooler lava crust emissivity (ε_{crust}) is different than that of the molten lava emissivity (ε_{hot}):

$$\varepsilon_{eff} = \varepsilon_{crust} f_{crust} + \varepsilon_{hot}(1 - f_{crust}) \quad \text{(eq. 5)}$$

This differs from previous FLOWGO modeling that assumed only a single emissivity ($\varepsilon_{hot} = \varepsilon_{crust}$ = 0.95). Based on recent work by Ramsey and Harris [2016], Lee and Ramsey [2016] and Lee et al. [2010], the emissivity of molten lava in situ (ε_{hot}) and silicate glasses in the laboratory is likely much lower (avg. ~ 0.6) over the 5 – 25 μm TIR region. For the emissivity of the crusted surface (ε_{crust}), we use the same value (0.95) from prior studies [Harris, 2013]. Assuming this *two-component emissivity model,* therefore, results in a lower radiant heat loss for situations where the $f_{crust} < 1$. This should result produce a slower cooling flow and therefore, a greater cooling limited distance (maximum length). The lower emissivity of the molten fraction reduces its radiative efficiency; and hence, the control volume cools more slowly.

Results.

The two-emissivity model

To estimate the maximum difference in the cooling limited distance between the two emissivity models, we first ran PyFLOWGO with a constant slope of 5°, crust temperature and crust fraction down the entire flow length. The simulations are shown between an uncrusted flow (f_{crust} = 0) with an effective emissivity of 0.6 and a fully crusted flow (f_{crust} = 1) with an effective emissivity of 0.95; as well as a flow that is half crusted (f_{crust} = 0.5) having an effective emissivity of 0.78. The maximum difference between the two models is expected to be between the uncrusted and the fully crusted flows. Results show a linear relationship between crust cover/emissivity to the final modeled flow distance. The *two-component emissivity model*

produces flows that are a maximum of 34% longer than flows using a single constant emissivity (Figure 7). The difference in cooling limited distance here is only dependent on the crustal fraction, which is a function of flow velocity and directly related (i.e., the complement) to the fraction of molten material having the lower emissivity.

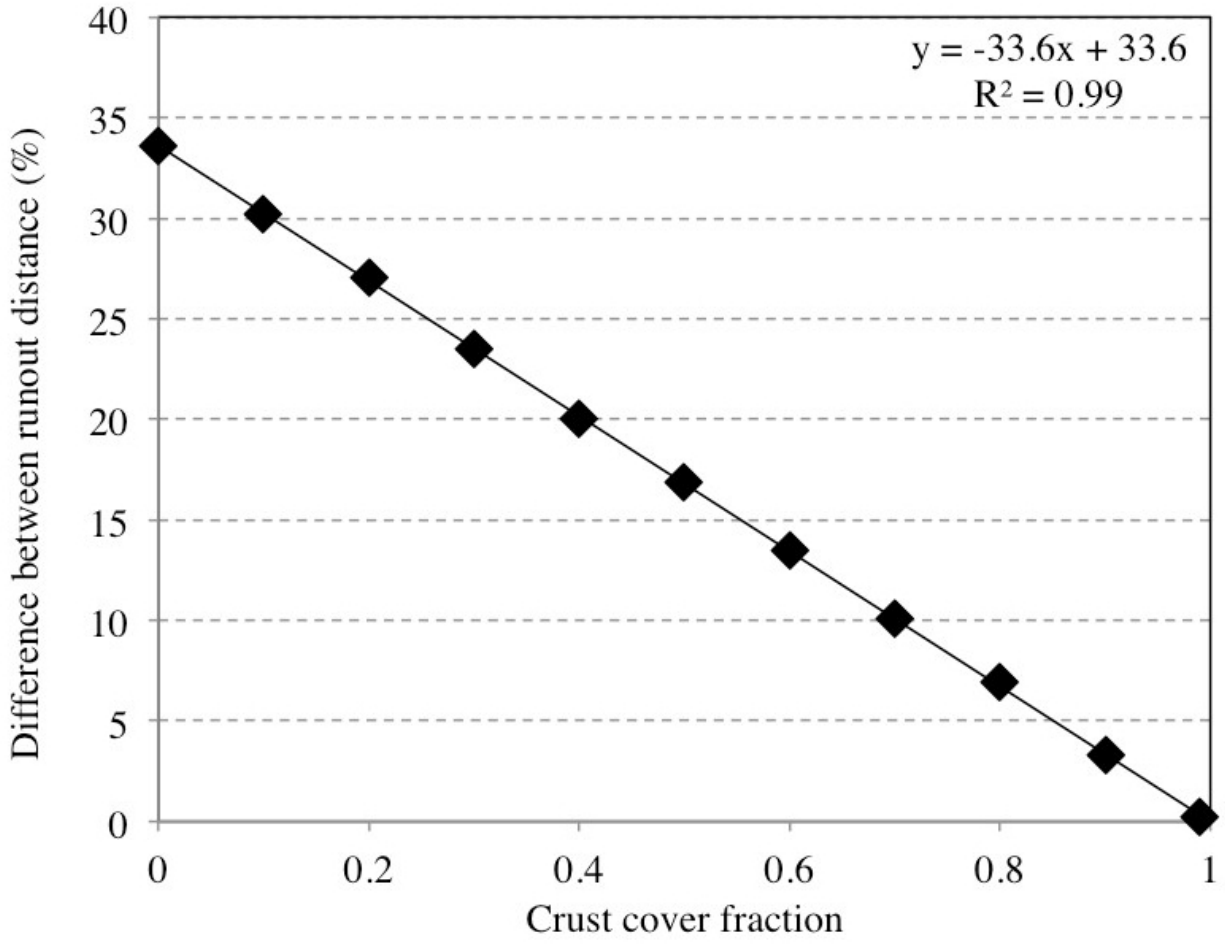


Figure 7. Percent difference between the run-out distances of the PyFLOWGO simulations using a 2-component emissivity model (ε_{hot} = 0.6 and ε_{crust} = 0.95) versus a single emissivity model (ε_{hot} = ε_{crust} = 0.95) as function of crust cover fraction. There is no difference in run-out distances if the flow is fully crusted. By contrast, if initially uncrusted, the maximum difference is 33%. Crust temperature plays a minor role, but those changes do not exceed the symbol size on the figure.

525 *Petrology*

526 We analyzed the whole rock composition of two samples which were sampled from the lower,
527 folded region of the Cone II flow and near the terminus of the Leningradskoye Flow (Table 2).
528 The Leningradskoye flow sample is broadly consistent with reported values [e.g., Gordeev et al.,
529 2013; Belousov et al., 2015; Plechov et al., 2015]. The results from the Cone II flow sample,
530 however, do vary somewhat from those of the later stage northern vents reported by Fedotov et
531 al., [1991]. Our results show lower Al_2O_3 and higher in CaO and MgO, each by ~2 wt. %. These
532 variations would still classify the sample as basaltic, but are more consistent with the Fedotov et
533 al. [1991] results for the earlier stages of this eruption, which were emplaced before the Cone II
534 flow. These compositions were used for the petrologically-dependant fluid viscosity model used
535 by PyFLOWGO (Tables 2 and 3).

536

537 *The 2012 Leningradskoye Flow (TFE-50 eruption)*

538 Using MIROVA, we calculate that the TFE-50 eruption radiated approximately 5.87 (±1.76)
539 × 10^{16} J into the atmosphere during the course of the eruption. Application of eq. 3 to the
540 Tolbachik MODIS data, suggests that the TADR peaked at the very beginning of the eruption
541 reaching 300 (±100) m^3 s^{-1} on 29 November 2012 at 01:09 UTC. Later, the eruption showed a
542 progressive decline in intensity, with effusion rates dropping to 278 m^3/s on 1 Dec 2012, less
543 than ~100 m^3 s^{-1} on 13 December 2012, ~50 m^3 s^{-1}, on 22 January 2013, and ~5 m^3 s^{-1} by 22
544 August 2013 (Figure 4). These values correspond closely to those derived from visual mapping
545 of the flow field using the higher resolution ASTER/ALI data (Table 1).

546

MODEL NAME	MODEL CHOICE		REFERENCE
"crystallization_rate_model"	basic		Harris and Rowland (2001) and Chevrel et al. (2018)
"melt_viscosity_model"	vft		Giordano et al. (2008)
"relative_viscosity_model"	er		Einstein-Roscoe model from Chevrel et al. 2018
"yield_strength_model"	ryerson		Ryerson et al. (1988)
"crust_temperature_model"	constant		Harris and Rowland (2001) and Chevrel et al. (2018)
"effective_cover_crust_model"	basic		Harris and Rowland (2001) and Chevrel et al. (2018)
"vesicle_fraction_model"	constant		Harris and Rowland (2001) and Chevrel et al. (2018)
HEAT BUDGET CONTRIBUTION	**MODEL CHOICE**		**REFERENCE**
"radiation" / radiation (2 emissivity)"	yes		This study
"condution"	yes		Harris and Rowland (2001)
"forced convection"	yes		Harris and Rowland (2001)
"rain"	no		Harris and Rowland (2001)
"viscous heating"	no		Harris and Rowland (2001)
PARAMETERS	**VALUE**	**UNITS**	**REFERENCE**
"step_size"	10	m	Harris and Rowland (2001) and Chevrel et al. (2018)
"effusion_rate"	278	m^3/s	from MODIS (this study)
"width"	30	m	ALI image data (this study)
"depth"	6.1	m	this study- best fit
"gravity"	9.81	g/m^2	
"eruption_condition"			
"eruption_temperature"	1355.15	K	Plechov et al. (2015)
"lava_state"			
"crystal_fraction"	0.25		Plechov et al. (2015)
"density_dre"	2630	kg/m^3	Volynet al. (2015)
"vesicle_fraction"	0.06		Plechov et al. (2015)
"radiation_parameters"			
"stefan-boltzmann_sigma"	5.67E-08	$W/m^2 K^4$	stefan-boltzmann constant
"emissivity_epsilon_crust"	0.95		this study
"emissivity_epsilon_uncrusted"	0.6		Lee and Ramsey (2016)
"conduction_parameters"			
"basal_temperature"	773.15	K	Harris and Rowland (2001) and Chevrel et al. (2018)
"core_base_distance"	19		Harris and Rowland (2001) and Chevrel et al. (2018)
"convection_parameters"			
"wind_speed"	5	m/s	Harris and Rowland (2001) and Chevrel et al. (2018)
"ch_air"	0.0036		Harris and Rowland (2001) and Chevrel et al. (2018)
"air_temperature"	273.15	K	Harris and Rowland (2001) and Chevrel et al. (2018)
"air_density"	0.4412	kg/m^3	Harris and Rowland (2001) and Chevrel et al. (2018)
"air_specific_heat_capacity"	1099	J/kg K	Harris and Rowland (2001) and Chevrel et al. (2018)
"thermal_parameters"			
"buffer"	140	°C	Harris and Rowland (2001)
"crust_cover_fraction"	0.9		this study: best fit
"alpha"	-0.16		this study: best fit
"crust_temperature"	773.15	°C	Belousov et al. (2015)
"melt_viscosity_parameters"			
"a_vft"	-4.55	Pa s	Volynet al. (2015)
"b_vft"	6887.303	J/mol	Volynet al. (2015)
"c_vft"	527.44	K	Volynet al. (2015)
"crystals_parameters"			
"crystals_grown_during_cooling"	0.37		this study: best fit
"solid_temperature"	1253.15	K	this study: best fit
"latent_heat_of_crystallization"	350000	J/kg	Harris and Rowland (2001) and Chevrel et al. (2018)

Table 3. All PyFLOWGO input models and parameters that were used for the Leningradskoye lava flow of the 2012 Tolbachik eruption.

549 Because the ASTER GDEM is created from all ASTER scenes spanning from 2000 – 2011,
550 it does not resolve the TFE-50 eruption lava flow fields. The ASTER single scene DEM created
551 from the 11 Jan 2018 acquisition, however, was relatively free of these data errors and
552 represents the surface five years following the TFE-50 eruption. This DEM was precisely
553 geolocated to the ASTER GDEM, which was then subtracted from it. The outlines of the flow
554 fields are resolved as a positive elevation anomaly. Transects taken perpendicular to the
555 Leningradskoye Flow show steep levees and flow fronts with maximum thicknesses of 35 m. In
556 some of these transects, the channel is visible and ranges from 30-50 m in width and 5 – 20 m
557 in depth. It was not possible, however, to discern the channel at the vent, perhaps because it
558 had been filled in by subsequent flow activity. A transect down this flow varies in average
559 thickness from 46 m near the vent to 16 m over the rest of the flow.
560 PyFLOWGO was run to simulate the Leningradskoye lava flow that formed between 29 Nov
561 2012 and 1 Dec 2012. In that period, the flow was fed by an open channel and reached a length
562 of 11.3 km, which is 70% of its final length. After 1 Dec 2012, the effusion rate dropped and later
563 lava tubes formed allowing the flow to extend to its final length (16.4 km). We did not attempt to
564 fit the final flow length because PyFLOWGO is designed only for open channel systems. We use
565 the effusion rate for this time period determined by MIROVA (278 m^3/s) for model initialization
566 and the steepest line of descent measured on the pre-flow ASTER GDEM. The active channel
567 widths are measured directly from the ALI and ASTER infrared data. These are likely
568 overestimates, however, due first to the minimum spatial resolution of 30 m/pixel (ALI) and 15
569 m/pixel (ASTER VNIR) and, second, to the intense radiance, which where convolved with an
570 instrument's point spread function, causes excess radiance to be detected in the surrounding
571 lava-free pixels. This results in the channel-related thermal anomaly to appear wider than the

572 actual widths measured in the field. The effect was most noticeable in the upper part of the flow
573 where the emitted radiance was most intense. The channel width at the vent was therefore set
574 to 30 m, the minimum resolvable distance in the ALI data and the ASTER DEM. To match the
575 effective MIROVA effusion rate over the at-vent slope, the depth is set at 6.1 m, which is in
576 agreement with field-based estimates [Belousov et al., 2015]. Some PyFLOWGO input
577 parameters were obtained by information obtained during the eruption [e.g., Plechov et al., 2015,
578 Volynet et al., 2015; Gordeev et al., 2015; Belousov and Belousova, 2018] or by assumptions
579 based on other well-constrained basaltic flows following Harris and Rowland [2001] and Chevrel
580 et al. [2018]. For example, to estimate the initial viscosity we consider the petrologic observations
581 from Plechov et al. [2015], which include the interstitial glass composition having 0.03 wt. %
582 H_2O, and the cooled lava having an average of 25 vol. % crystals and 6 vol. % bubbles. We used
583 the model of Giordano et al. [2008] for the interstitial melt viscosity in association with the
584 Einstein-Roscoe model for computing the effect of crystals. Because the vesicle fraction is as
585 low as 6 vol. %, the effect of bubble on viscosity is neglected here. Model results produced an
586 initial viscosity of 1.9×10^4 Pa·s at the eruption temperature of 1082 °C, which is in agreement
587 with field estimations and measurements done by Gordeev et al., 2015 and Belousov and
588 Belousova, 2018]. The simulation that best fit the flow length constrained by the channel widths
589 and emitted radiance down-flow measured from the ALI image was produced using the
590 parameters reported in Table 3 and is presented in Figure 8.
591

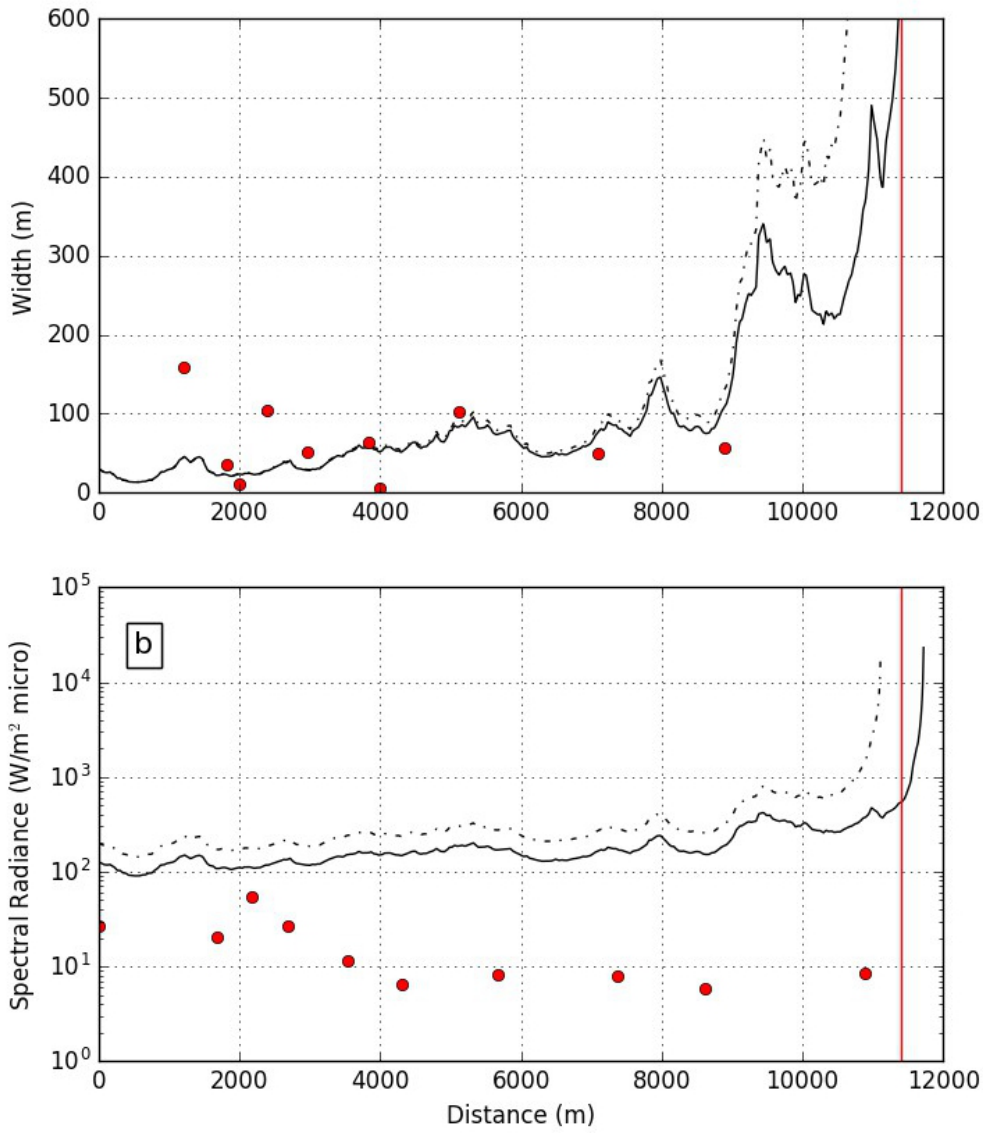


Figure 8. Best fit FLOWGO simulation for the Leningradskoye lava flow of the 2012 Tolbachik eruption using input models and parameters given in Table 3. The continuous line is for a two-component emissivity model, whereas the dashed line represents a singular emissivity of 0.95. The red dots are channel width measurements from ASTER and ALI images. The vertical red lines represent the flow length on 1 Dec 2012 measured from the ALI image. (A) Modeled channel width. Misfits near the beginning of the flow are likely due to the intense radiance from the lava in these regions causing the channels to appear larger than their actual width due to radiance bleeding into neighboring pixels. (B) Modeled emitted radiance. Misfits at greater distances here are likely due to increasing percentages of cooled crust/older lava mixing within these pixels.

The best fit model result used a variable crustal coverage as part of the "basic" model in PyFLOWGO, originally proposed by Harris and Rowland [2001]. This model allows f_{crust} to increase as a function of mean flow velocity (V_{mean}):

$$f_{crust} = f_{init}\, e^{\alpha V_{mean}} \quad \text{(eq. 6)}$$

where f_{init}, the initial (at vent) crust fraction and α, a coefficient, were derived for a poorly insulated flow by Harris and Rowland [2001] to be 0.9 and -0.16, respectively. The velocity of the lava within the channel varied between 2 and 3.5 m/s within the first kilometer and then

progressively decreased down-flow (Figure 9d). These values are also in agreement with field-based estimates reported in Belousov et al. [2015].

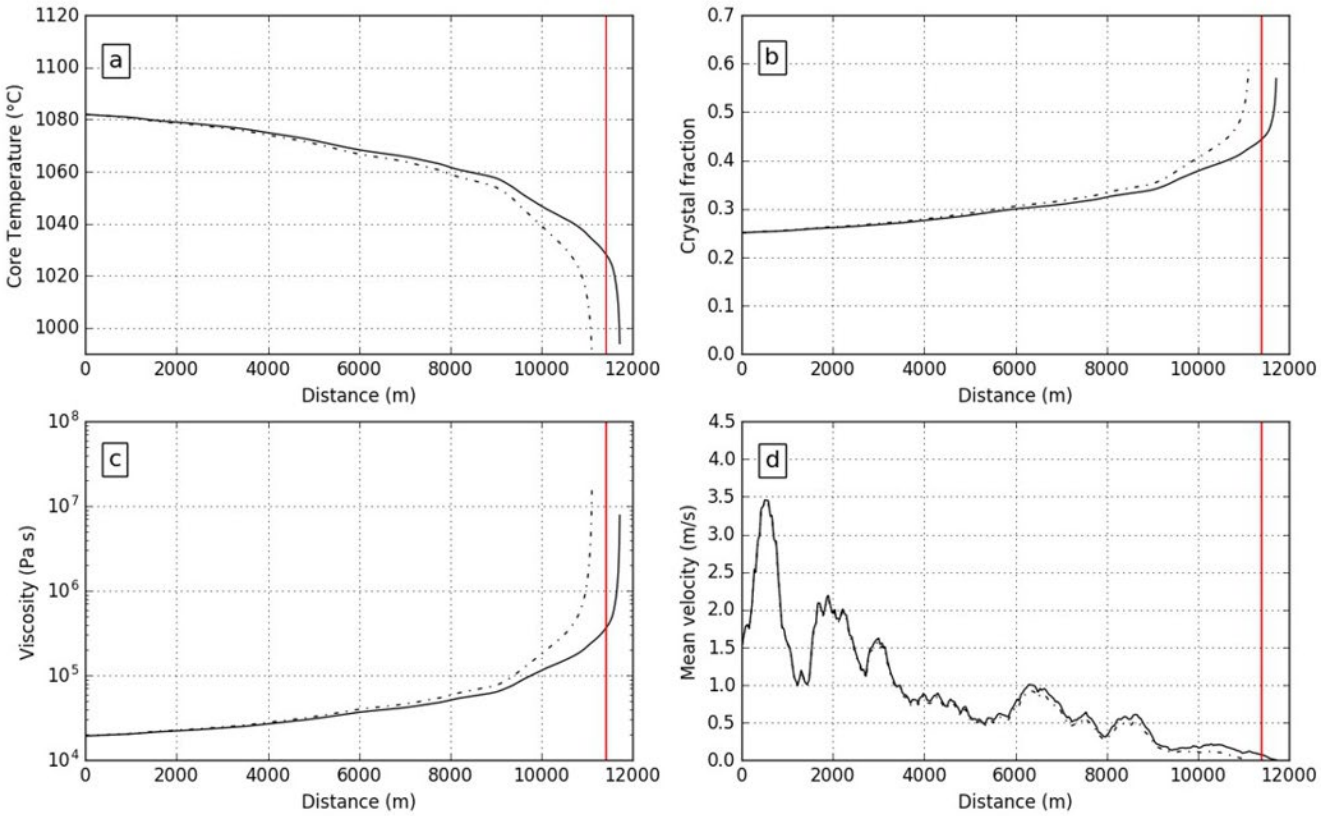


Figure 9. Thermo-rheological variations for the 2012 Leningradskoye lava flow properties using the best fit simulation and the input models and parameters given in Table 3. The continuous line is the two-component emissivity model results, whereas the dashed line represents a singular emissivity of 0.95. The vertical red lines represent the flow length on 1 Dec 2012 measured from the ALI image. The singular emissivity produces model results that consistently over-predict the actual flow length.

In these simulations, the difference between the single and the two-component emissivity is small because the modeled crust coverage fraction is high, varying from 60% – 90%. (Figure 10). This range is somewhat higher than seen in the field images of the open channel, which varied between 35% – 60% (Figure 2). However, the field-based values are derived from the visibly darker fraction of crust on the channel surface. It is possible that the “radiative crust” (i.e., surfaces that are still visibly red but have cooled enough to raise the emissivity) is higher.

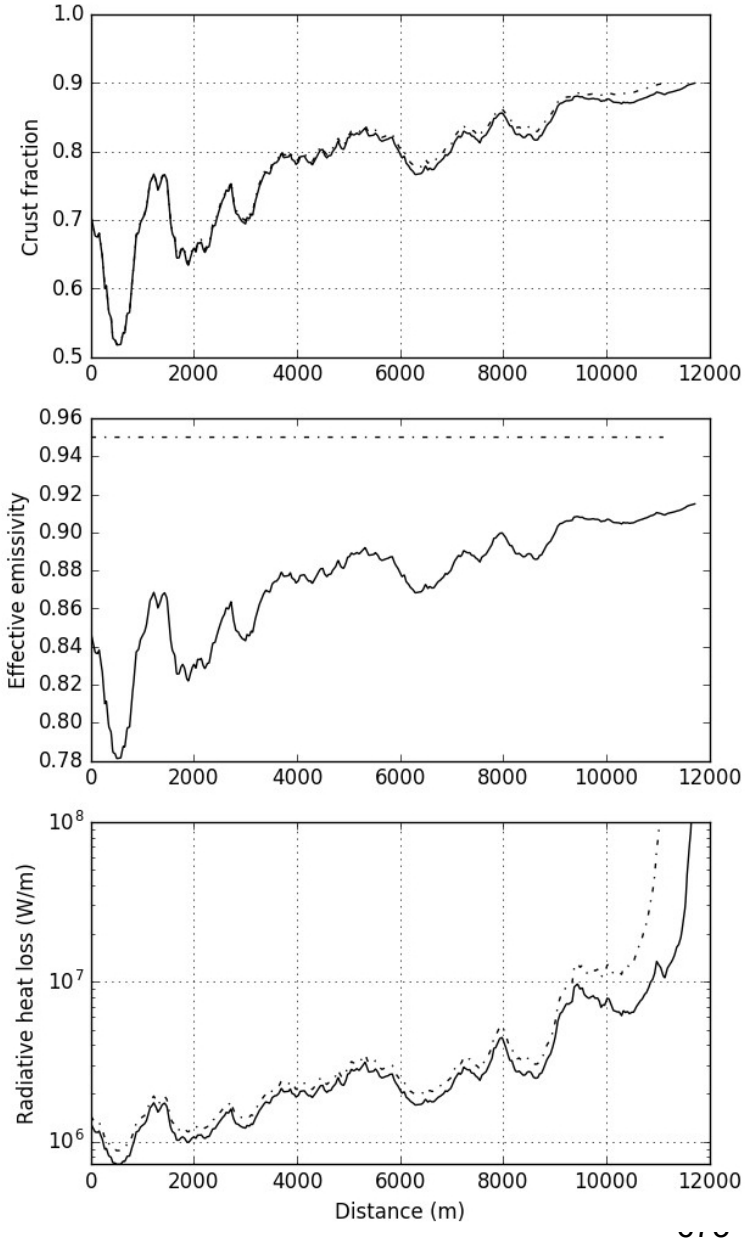


Figure 10. Variations in the crustal coverage, effective emissivity and radiative heat loss for the 2012 Leningradskoye lava flow properties using the best fit simulation and the input models and parameters given in Table 3. The continuous line is the two-component emissivity model results, whereas the dashed line represents a singular emissivity of 0.95.

We also attempted to fit the spectral radiance obtained from the ALI data to the model-output for emitted spectral radiance from the simulated PyFLOWGO surface. Unsaturated pixel-integrated spectral radiance values were extracted down-flow (Figure 6a) from the ALI band 7 (0.87 μm). The subpixel hot fraction emitted radiance was estimated using the two-component mixing approach of Dozier [1981] and then compared to the PyFLOWGO model output (Figure 8b). The results show that the two-component emissivity model does result in a spectral radiance that is closer to that of the ALI data. However, the fit deteriorates down-flow with the measured radiance decreasing to a near constant value, approximately an order of magnitude lower than the PyFLOWGO model predicted values. This overestimation by the model could be due to several factors. The ALI data are resampled during the conversion from the original radiance data (L1R) to the distributed L1Gst data product. This could cause mixing of radiant energy from

adjacent pixels containing cooled lava or snow, thus lowering the pixel-integrated values. Furthermore, the ALI data have not been atmospherically corrected. There were significant steam plumes and clouds encroaching on the upper part of the flow and smaller vapor plumes are seen emanating from the lava channel along the entire length. This atmospheric interference will lower the pixel integrated radiance [see Sawyer and Burton, 2006]. Finally, whereas PyFLOWGO calculates emitted radiance based on the hottest lava temperature at a particular point along the flow, the satellite data captures emitted energy from all temperatures within a given pixel. It is very likely that within a 30 m pixel, there exists some fraction of hot material plus that of cool/cold material, as well as numerous surfaces at temperatures between these two end-member temperatures [Dozier, 1981; Rothery et al., 1988; Harris, 2013]. These would not be resolved in the two-component subpixel analysis and yet would lower the effective pixel-integrated spectral radiance. Therefore, use of spectral radiance as a constraint on PyFLOWGO model output is best applied to higher-resolution (i.e., ground- or airborne) data together with in situ measurements of the intervening atmosphere.

The 1975 Cone II Flow (GTFE eruption)

The Cone II flow dimensions are easily resolved in the ASTER GDEM making it much more straight forward to measure the channel width and depth down-flow. Six perpendicular transects were taken from the base of Cone II the point where the flow spreads laterally and folding masks the end of the channel. The channel averaged 140 m in width and 11.8 m in depth over the six transects. At the base of Cone II, the channel is between 60-90 m wide and 8-9 m deep. These values are used as bounding constraints for initiation of PyFLOWGO (Table 4).

MODEL NAME	MODEL CHOICE		REFERENCE
"melt_viscosity_model"	basic		Giordano et al. (2008)
PARAMETERS	**VALUE**	**UNITS**	**REFERENCE**
"effusion_rate"	700, 1250	m^3/s	this study- best fit (see crust fraction below)
"width"	70	m	ASTER GDEM – this study
"depth"	8.7	m	this study- best fit
"eruption_temperature"	1325.15	K	Fedotov et al. (1991)
"viscosity_eruption"	50000	Pa s	this study- best fit
"crystal_fraction"	0.20		Fedotov et al. (1991)
"thermal_parameters"			
"crust_cover_fraction"	0.9, 0.4		this study: best fit

Table 4. Specific PyFLOWGO input models and parameters that differ from those in Table 3 that were used for the Cone II lava flow of the 1975 Tolbachik eruption.

This flow extended 5 km and was characterized by a very wide channel, oversteepened levees and a folded terminus with a 50 m high flow front. The morphology of the flow makes it appear perhaps more silicic than the actual composition, which is magnesian, moderately alkaline basalt [Fedotov et al., 1991]. Samples acquired from this flow in 2005 were found to be basalt with 50.5 wt. % SiO_2 (Table 2). Although the composition is basaltic, the effective viscosity was estimated in the field to range between 10^4-10^7 Pa·s and up to 10^9 Pa·s, based on lava flow front velocities [Vende-Kirkov, 1978; Fedotov et al. 1991].

To simulate the evolution of the thermo-rheological properties down-flow, we used the same input parameters as used for the 2012 Leningradskoye lava flow but imposed an initial melt viscosity on the low-end (5 x 10^4 Pa·s) of the range provided by Vende-Kirkov [1978] together with an eruption temperature of 1050 °C [Fedotov et al., 1991]. We were able to fit the channel width and the final length with an effusion rate of 700 m^3/s and an initial channel dimension of 70 × 8.7 m (Figure 11). The difference between the two-component emissivity model and the single emissivity model was negligible considering the high initial crust cover fraction of f_{init} = 0.9 used (Figure 12). However, the large channel and thickness of this flow indicates a higher initial effusion rate and flow velocity could have been possible. In a case like this, a similar model

fit can be obtained with a higher effusion rate (1250 m^3/s) using a similar initial channel size (70 x 8 m), but starting with a lower crustal coverage (f_{init} =0.4) and the two-component emissivity model. For this case, it is critical to consider the two-component emissivity model as it has a significant impact on the final results (Figures 11-13). In particular, using the single emissivity model generated a much shorter flow (4000 m) where the viscosity increased to 10^8 Pa·s (Figure 13c). Fedotov et al. [1991] estimated the flow velocity to be ~0.3 m/s approximately 2.5 km from the vent, whereas Belousov et al. [2015] reported < 0.2 m/s. The modeled velocity of the lava within the channel is estimated here to be 1.5 to 2 m/s near the vent, decreasing to < 0.5 m/s after the first kilometer, which is in good agreement with the prior estimates.

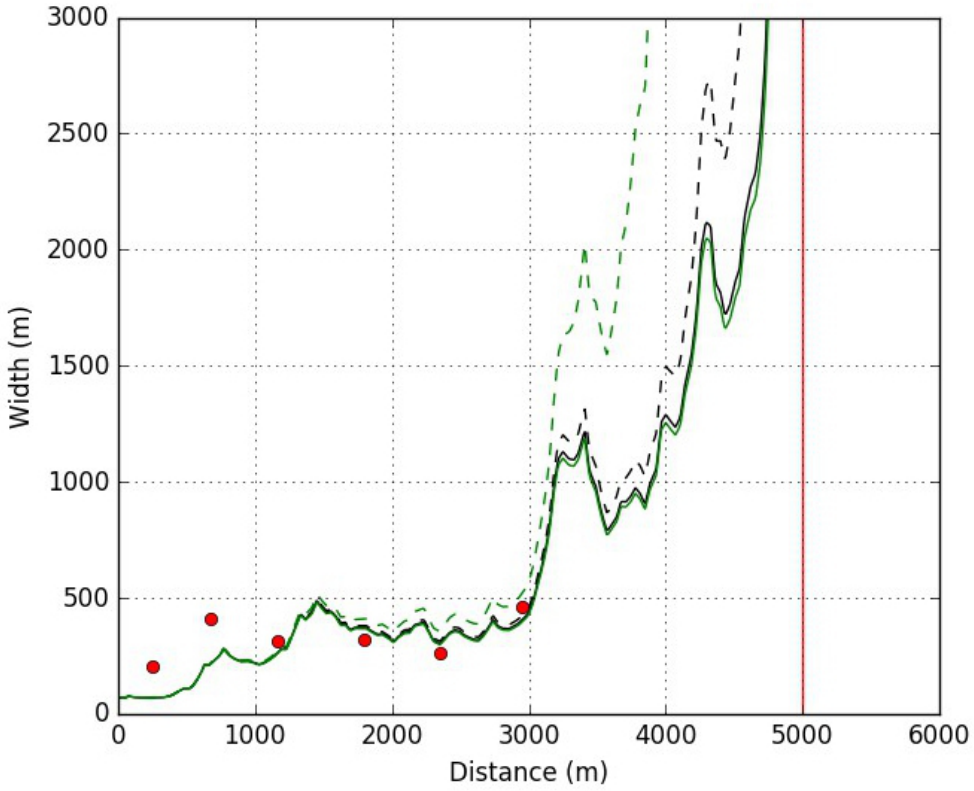


Figure 11. Best fit PyFLOWGO simulation for the Cone II lava flow emplaced during the 1975 Tolbachik eruption. Input models and parameters are similar to those used for the 2012 eruption, except those presented in Table 4. The green lines show the results for an effusion rate of 1250 m^3/s and an initial crust fraction (f_{init}) of 0.4, whereas the black lines are for an effusion rate of 700 m^3/s and f_{init} = 0.9. The solid lines represent the two-component emissivity model results, whereas the dashed lines represent a singular emissivity of 0.95. The red dots are width measurements from ASTER GDEM data and the vertical red line represents the final flow length.

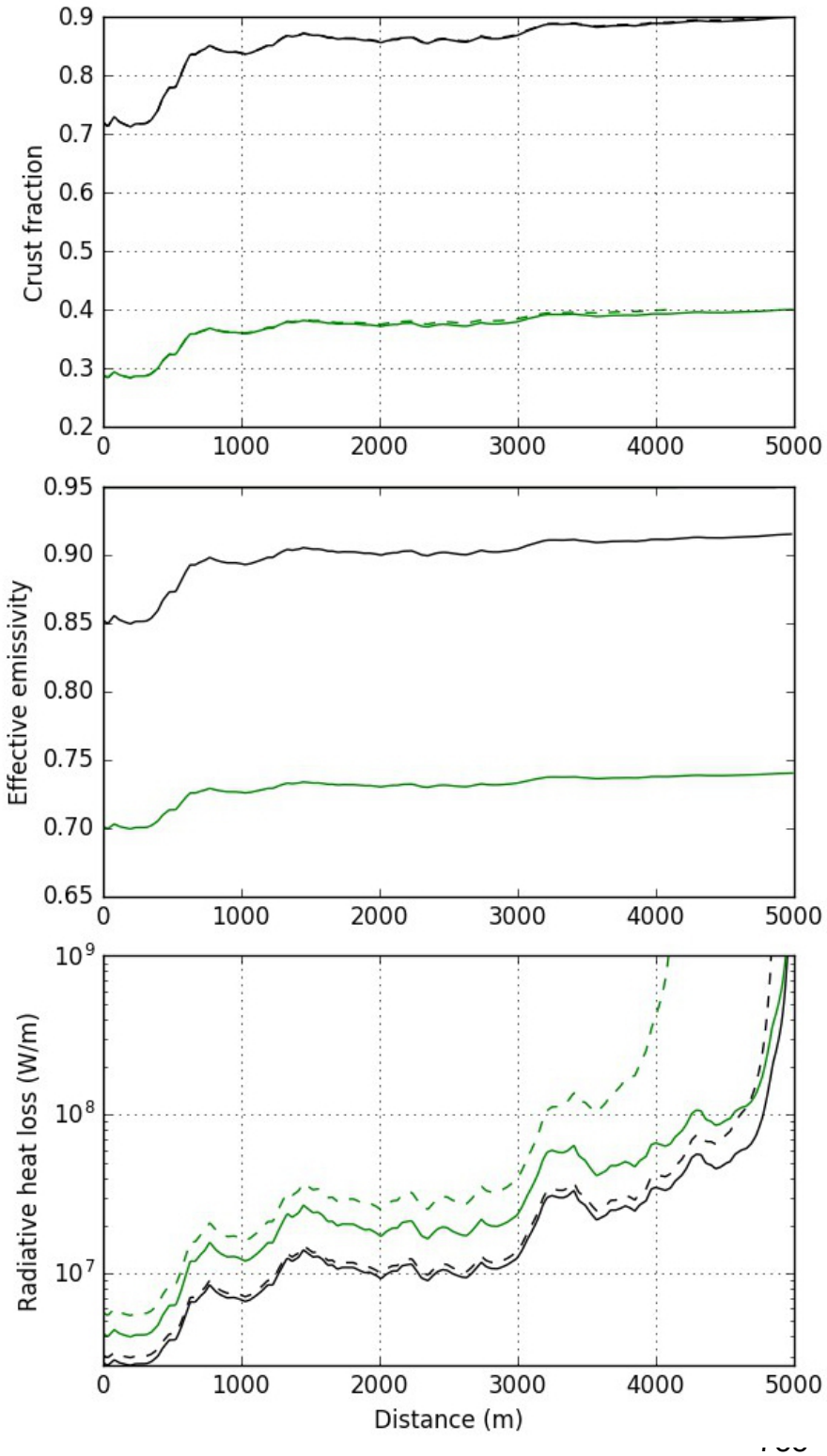


Figure 12. Variations in the crustal coverage, effective emissivity and radiative heat loss for the 1975 Cone II lava flow properties using the best fit simulation and the input models and parameters given in Table 3. The green lines show the results for an effusion rate of 1250 m^3/s and an initial crust fraction (f_{init}) of 0.4, whereas the black lines represent an effusion rate of 700 m^3/s and f_{init} = 0.9. The solid lines are the two-component emissivity model results, whereas the dashed lines are for the singular emissivity of 0.95.

Discussion.

The 2012-2013 eruption produced high effusion rate channelized basaltic flows useful for testing and refining the PyFLOWGO modeling. Because of a unique set of high-resolution orbital assets and data acquisition programs ongoing at the time of the eruption, unprecedented TIR data coverage exists throughout all phases of this eruption. These were useful to constrain channel lengths and widths, vent locations, temperature, as well as multispectral emissivity of molten surfaces and channel depths from digital elevation models (DEMs). This

information, combined with the detailed reporting from Russian scientists present during the eruption, were used to initiate PyFLOWGO modeling of the largest channelized flow, which formed near the very start of the eruption. With the ability to refine and calibrate the model using those additional satellite data, the best-fit model parameters were then applied to the large 1975 Cone II flow to investigate the impact of assumed parameters such as emissivity on PyFLOWGO.

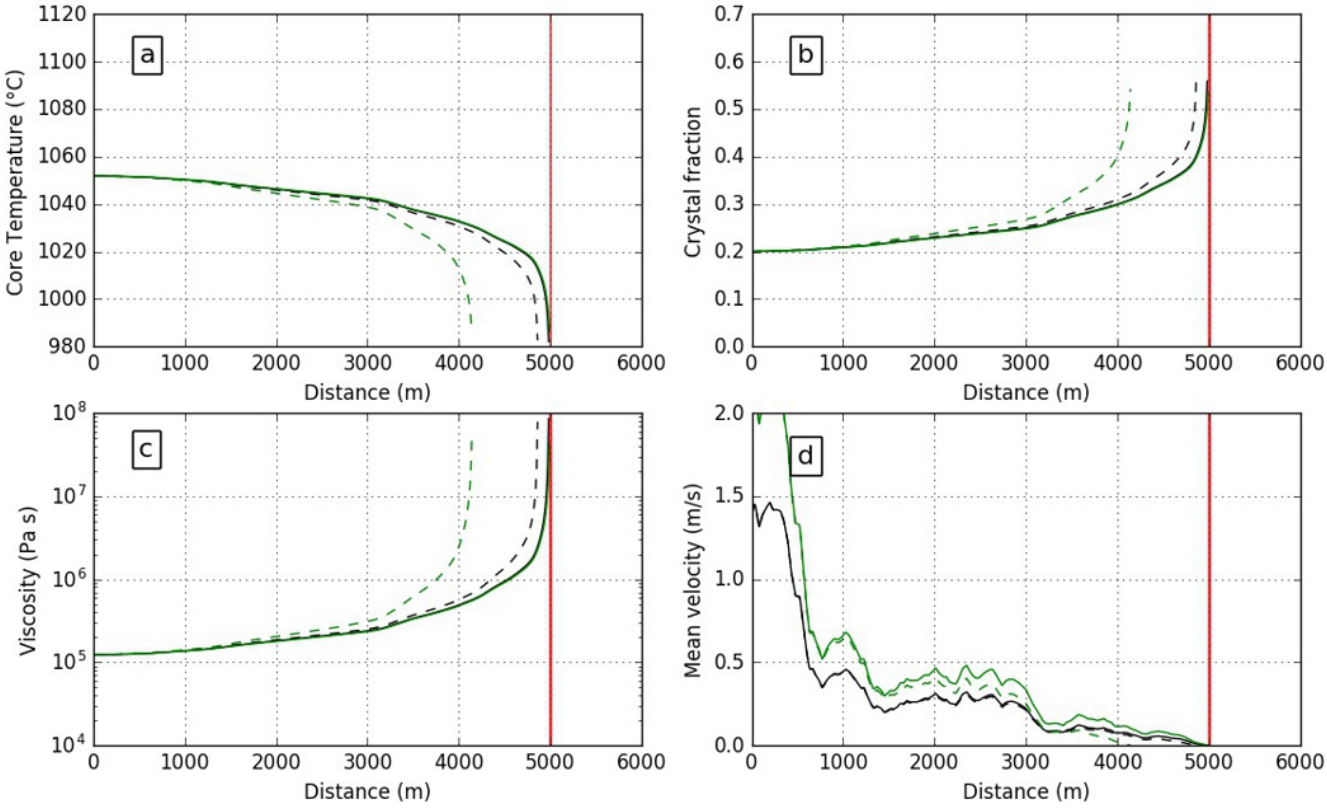


Figure 13. Thermo-rheological variations for the 1975 Cone II lava flow properties using the best fit simulation. The input models and parameters are similar to those used for the 2012 eruption, except the few presented in Table 4. The green lines show the results for an effusion rate of 1250 m^3/s and an initial crust fraction (f_{init}) of 0.4, whereas the black lines represent an effusion rate of 700 m^3/s and f_{init} = 0.9. The solid lines represent the two-component emissivity model results, whereas the dashed lines are a singular emissivity of 0.95. The vertical red lines represent the final flow length on 1 Dec 2012 measured from the ALI image.

The PyFLOWGO model provides a great degree of flexibility on many of the input variables and choice of viscosity models. This flexibility also constraining the model output quite difficult

807 without knowledge of at least some of the input parameters, and highlights the need for
808 independent flow parameter data against which to best-fit model-driven scenarios. Past studies
809 using FLOWGO modeling commonly compared the results to well-constrained field data, such
810 as the channel dimensions, measurements of the crust percentage, velocity and/or cooling
811 profiles down-flow [Harris et al., 2007b; Wright et al., 2008, Harris and Rowland, 2009, 2012].
812 Here, we apply PyFLOWGO, constrained primarily by high spatial (e.g., ASTER and ALI) and
813 high temporal (e.g., MODIS) resolution satellite data. The MODIS time-averaged discharge rate
814 and the ASTER-derived DEM data proved to be the most important as they provide the volume
815 flux source term, and topographic underlay required by the model, respectively. The ASTER/ALI
816 data also allowed the flow length, channel widths, advance rate, temperature and spectral
817 radiance to be constrained to some degree.

818 Two parameters measured from the high spatial resolution data (channel width and spectral
819 radiance) proved more difficult to constrain. The excessive radiance from the wider, less crust-
820 covered channels closer to the vent resulted in overestimations of the measured channel widths.
821 Conversely, channelized regions with a modeled crust percentage greater than ~75% had
822 emitted spectral radiance much lower than the PyFLOWGO predictions. Incomplete atmospheric
823 correction, image resampling and pixel mixing likely produces emitted radiance values at scales
824 too complex to be extracted from the 30 m pixels examined here; an issue that warrants future
825 study.

826 Despite the paucity of constrained ground-based data and the complexities regarding higher-
827 level modeling of some of the high resolution image data, we were able to model the
828 Leningradskoye lava flow by fitting the final flow length and starting discharge rate. Model output
829 of core temperature, crystal fraction, mean velocity and viscosity are in good agreement with

ground and satellite control. Applying these constraints then to the Cone II flow combined with data extracted from the ASTER GDEM allowed us to estimate the discharge rate as well as the effect of variable emissivity and initial crust cover. The difference between two-component and the single emissivity models was negligible where considering a high initial crust cover fraction, but significant for higher effusion rate with a lower initial crust cover fraction (Figures 12-13). Such a validation approach is important for interpreting older flows where information on their emplacement is either limited or nonexistent.

The primary focus of this study was to apply PyFLOWGO using data constrained as much as possible by only satellite data, and in the process, test one variable (emissivity), which has always been assumed constant in past studies. We modified PyFLOWGO to accept two values for emissivity and assigned those to the crust and molten fractions in the channel. The effective emissivity term was thus a weighted sum of the crust fraction having a high emissivity (0.95) plus the molten fraction having the lower emissivity (0.60). This change has a measureable (linear) impact on the PyFLOWGO results for a theoretical flow and where applied to the actual Tolbachik flows resulted in a slightly improved fit for the 2012 Leningradskoye flow and significantly improved fit for the 1975 Cone II flow. As one might expect, the largest change in the model results arises where a flow initially enters the channel free or nearly free of cooling, higher emissivity crust. If a flow is modeled with a high initial crust fraction, the two end-member emissivity modification will only provide a marginally better final fit. However, what we did not explore here is assumption in PyFLOWGO that crust formation is related solely to flow velocity rather than temperature. A more complex solution incorporating crust formation with flow cooling (modulated by the lower emissivity) is warranted. Field images of the 2012 flow channels commonly showed significantly less crust at a given position along the flow than was predicted

by PyFLOWGO. If this is the case, then we predict the lower emissivity of the molten fraction of the channel will have more of an impact.

The emissivity measurement of molten material has been presented in numerous recent studies both in the laboratory and the field [Ramsey and Harris, 2016; Lee and Ramsey, 2016; Lee et al., 2010; Abtahi et al., 2002]. The assessment of Burgi et al. [2002] for the emissivity of the surface of the active lake at Erta Ale (0.74), albeit in the 1.1-1.7 μm region, is in agreement with this study [see also Flynn et al. 2001]. This fundamental change in our understanding of how efficiently materials radiate heat prior to solidifying is important for models such as PyFLOWGO but also in any situation where an accurate thermal infrared non-contact temperature is made. Emissivity measured over multiple wavelengths produces a spectrum that relates information about the material's petrology, its state of atomic bond vibrations and angles, and the amount of glass formation [see Ramsey and Fink, 1999]. The broadband emissivity, an average over the entire wavelength region, is a measure of how efficiently that material emits heat. It should be noted that the prior studied of molten emissivity were conducted in the TIR region (~ 5 – 25 μm in the laboratory and ~ 8 – 12 μm in the field/from orbit). Radiant heat loss, however, is occurring over a larger portion of the electromagnetic spectrum, most notably in the short-wave infrared region (~ 1 – 5 μm). If the emissivity is closer to unity at these wavelengths, then the impact of the lower emissivity in the thermal infrared region will be mitigated to a degree. Further laboratory studies of emissivity in the 1-5 and 8-14 μm regions are planned to clarify this question. Further study into the model's logic of linking crust formation to velocity rather than temperature is also planned. This is likely resulting in an underestimate of the effect of the two end-member emissivity approach. More model simulations with this logic changed to temperature or temperature/velocity dependency are planned.

Conclusions.

The 2012-2013 TFE-50 eruption of Tolbachik volcano produced several large basaltic flow fields containing large open channel flows. The largest of these was the Leningradskoye flow, which was emplaced in the early days of the eruption. The active period of this eruption was captured by high spatial resolution VNIR to TIR image data from ASTER and ALI as well as high temporal resolution, low spatial resolution image data from MODIS. The ASTER and ALI data allowed the lava flow progress and flow field areal extent/volumes to be tracked, whereas the MODIS data provided estimates of the lava time-averaged discharge rates. Using these datasets as a means to constrain the input parameters of PyFLOWGO we were able to model the Leningradskoye flow as it appeared on 1 Dec 2012. Over the flow length of 11.3 km on that date, the core temperate was modeled to have decreased by ~80 °C down-flow, which resulted in an increase in viscosity from 10^4 to 10^7 Pa·s and crystal fraction from 25 vol. % to near 60 vol.%. Over the flow length, the crust cover varied from ~50% to > 90%, whereas the velocity decreased from 3.5 m/s to < 0.5 m/s near the flow terminus.

These input parameters were assumed to be similar for the 1975 Cone II flow. Here, the ASTER GDEM was used for channel width and depth constraints. The wide channel and greater flow thickness suggests a higher effusion rate feeding this event, which were shown by the PyFLOWGO results. The Cone II flow can be modeled to have a higher effusion rate (1250 m^3/s) and lower average crust coverage (~ 40%) than the Leningradskoye flow.

One important PyFLOWGO input parameter tested here was the effect of variable emissivity on flow cooling rates. We developed a new implementation of PyFLOWGO to account for a two-component emissivity model. This effective emissivity resulted in a measureable linear change in the model results and was strongly dependent on the crust fraction estimated by the model.

For the smaller and slower Leningradskoye flow, the crust fraction was higher at the start of the channel compared to the Cone II flow. This higher fraction of crust mitigates the impact of the lower emissivity for the molten fraction. This effect does, however, become an important factor for larger flows emplaced at higher velocities and lower degrees of crust cover.

Because the current implementation of all lava flow emplacement models tie crust formation to effective radiation temperature [Pieri et al. 1990], we argue that it is also appropriate to apply the two-end-member emissivity assumption. Such modifications, coupled with future studies of active channel-fed flow emplacement, will further constrain the uncertainties inherent in our understanding of lava flow heat loss and cooling dynamics.

Acknowledgements.

The research of MSR has focused on Kamchatka for over a decade supported by several NASA (NNX08AJ91G, NNX11AL29G, NNX14AQ96G) and NSF (1019558, 1524011) grants. This project evolved out of that past work and forms the basis for a new NASA planetary project funded under the SSW Program. MSR would like to thank the collaborators on those past projects whose work helped facilitate this study (A. Belousov, M. Belousova, E. Gordeev, J. Krippner and R. Wessels). MOC and AH acknowledge the Agence National de la Recherche through the project LAVA (Program: DS0902 2016; Project: ANR-16 CE39-0009, http://www.agence-nationale-recherche.fr/Projet-ANR-16-CE39-0009) for full support. This is ANR-LAVA contribution no. 9.

Bibliography.

Abrams, M., Bailey, B., Tsu, H., and Hato, M., The ASTER Global DEM, Photogram. Eng. Rem. Sens., 76, 344-348, 2010.

Abtahi, A.A., Kahle, A.B., Abbott, E.A., Gillespie, A.R., Sabol, D., Yamada, G., Pieri, D., Emissivity changes in basalt cooling after eruption from Pu'u 'O'o, Kilauea, Hawaii, Amer. Geophys. Union Eos Trans., abstract V71A-1263, 2002.

Ball, M. and Pinkerton, H. Factors affecting the accuracy of thermal imaging cameras in volcanology, J. Geophys. Res., 111, B11203. DOI: 10.1029/2005JB003829, 2006.

Belousov, A., Belousova, M., Edwards, B., Volynets, A., Melnikov, D., Overview of the precursors and dynamics of the 2012–13 basaltic fissure eruption of Tolbachik Volcano, Kamchatka, Russia, J. Volcanol. Geotherm. Res., 307, 22-37, 2015.

Bulletin Global Volcanism Network (BGVN), Tolbachik Volcano, Smithsonian Institution, Washington, D.C., December, 2012.

Burgi, P.-Y., Caillet, M. and Haefeli, S., Field temperature measurements at Erta 'Ale lava lake, Ethiopia, Bull. Volcanol., 64, 472-485, 2002.

Carter, A.J., Ramsey, M.S., Belousov, A.B., Detection of a new summit crater on Bezymianny Volcano lava dome: satellite and field-based thermal data, Bull. Volcanol., doi: 10.1007/s00445-007-0113-x., 2007.

Carter, A.J., Girina, O., Ramsey, M.S., Demyanchuk, Y.V., ASTER and field observations of the 24 December 2006 eruption of Bezymianny Volcano, Russia, Rem. Sens. Environ., 112, doi: 10.1016/j.rse.2007.12.001, 2569-2577, 2008.

Chevrel, M.O., Labroquère, J., Harris, A.J.L., Rowland, S.K., PyFLOWGO: An open-source platform for simulation of channelized lava thermo-rheological properties, Comp. Geosci., 111 (Supplement C), 167-180, 2018.

Coppola, D., Barsotti, S., Cigolini, C., Laiolo, M., Pfeffer, M.A., Ripepe, M., Monitoring the effusion rates, volumes and emplacement style of large lava flows using MODIS-MIROVA data: the case of the Holuhraun-Bárðarbunga 2014-2015 eruption, (this volume).

Coppola, D., Laiolo, M., Cigolini, C., Delle Donne, D., and Ripepe, M., Enhanced volcanic hot-spot detection using MODIS IR data: Results from the MIROVA system, in Harris, A.J.L., et al., eds., Detecting, Modelling and Responding to Effusive Eruptions: Geological Society of London Special Publication 426, p. 181–205, doi:10.1144/SP426.5, 2016.

Coppola, D., Laiolo, M., Piscopo, D., Cigolini, C., Rheological control on the radiant density of active lava flows and domes, J. Volcanol. Geotherm. Res., 249, 39–48, doi:10.1016/j.jvolgeores.2012.09.005.C, 2013.

Coppola, D., James, M.R., Staudacher, T., Cigolini, C.A., Comparison of field- and satellite-derived thermal flux at Piton de la Fournaise: Implications for the calculation of lava discharge rate, Bull. Volcanol., 72(3), 341-356, doi: 10.1007/s00445-009-0320-8, 2010.

Crisp, J., Kahle, A.B. and Abbott, E.A., Thermal infrared spectral character of Hawaiian Basaltic glasses, J. Geohpys. Res., 95(B13), 21657-21669, 1990.

Crisp, J., Baloga, S., A method for estimating eruption rates of planetary lava flows, Icarus, 85 (2), 512-515, 1990.

Crown, D.A. and Baloga, S.A., Pahoehoe toe dimensions, morphology, and branching relationships at Mauna Ulu, Kilauea Volcano, Hawai'i, Bull. Volcanol., 61 :288-305, 1999.

Dai, Chunli, Howat, I.M., Measuring Lava Flows With ArcticDEM: Application to the 2012–2013 Eruption of Tolbachik, Kamchatka, Geophys. Res. Lett. 44 (24), 12133-12140, 2017.

Davies, A.G., Chien, S., Tran, D., Doubleday, J., The NASA Volcano Sensor Web, advanced autonomy and the remote sensing of volcanic eruptions, in: Harris, A.J.L., De Groeve, T., Garel, F. and Carn, S.A. (eds.), Detecting, Modelling and Responding to Effusive Eruptions, Geol. Soc., London, Special Publications, 426, 137-158, 2016.

Digenis, C.J., Lencioni, D.E., Bicknell, W.E., New Millennium EO-1 Advanced Land Image, in Earth Observing Systems III, 3439, Int. Soc. Optics Photonics, 49-56, 1998.

Donegan, S.J. and Flynn, L.P., Comparison of the response of the Landsat 7 Enhanced Thematic Mapper Plus and the Earth Observing-1 Advanced Land Imager over active lava flows, J. Volcanol. Geotherm. Res., 135, 105-126, 2004.

Dozier, J., A method for satellite identification of surface temperature fields of subpixel resolution, Rem. Sens. Environ., 11, 221-229, 1981.

Dragoni, M., A dynamical model of lava flows cooling by radiation, Bull. Volcanol., 51, 88-95, 1989.

Dragoni, M., and A. Tallarico, Assumptions in the evaluation of lava effusion rates from heat radiation, Geophys. Res. Lett., 36, L08302,doi:10.1029/2009GL037411, 2009.

Duda, K.A., Ramsey, M., Wessels, R., Dehn, J., Optical satellite volcano monitoring: A multi-sensor rapid response system, in: P.P. Ho, (ed.), Geoscience and Remote Sensing, INTECH Press, Vukovar, Croatia, ISBN 978-953-307-003-2, 473-496, 2009.

Dvigalo, V.N., Svirid, I.Y., Shevchenko, A.V., The first quantitative estimates of parameters for the Tolbachik Fissure Eruption of 2012-2013 from aerophotogrammetric observations, J. Volcanol. Seismol., 8(5), 261-268, 2013.

Edwards, B.R., Belousov, A., Belousova, M., Melnikov, D., Observations on lava, snowpack and their interactions during the 2012-13 Tolbachik eruption, Klyuchevskoy Group, Kamchatka, Russia, J. Volcanol. Geotherm Res., 307, 107-119, 2015.Favalli, M., Pareschi, M., Neri, A. and Isola, I., Forecasting lava flow paths by a stochastic approach, Geophys. Res. Lett., 32, L03305, doi:10.1029/2004GL021718, 2005.

Fedotov, S.A., Balesta, S.T., Dvigalo, V.N., Razina, A.A., Flerov, G.B., Chirkov, A.M., New Tolbachik Volcanoes, Chapter 10, in Fedotov, S.A. and Masurenkov, Yu.P., (eds.), Active Volcanoes of Kamchatka - vol. 1, Nauka Publishers, Moscow, Russia, 214-279, 1991.

Flynn, L.P. and Mouginis-Mark, P.J., Cooling rate of an active Hawaiian lava flow from nighttime spectroradiometer measurements, Geophys. Res. Lett., 19(17), 1783-1786, 1992.

Flynn, L.P. and Mouginis-Mark, P.J., Temperature measurements of an active lava channel from spectral measurements, Kilauea Volcano, Hawaii. Bull. Volcanol., 56, 297-301, 1994.

Fujisada, H., Bailey, G.B., Kelly, G.G., Hara, S., Abrams, M.J., ASTER DEM performance, IEEE Trans. Geosci. Rem. Sens., 43(12), 2707-2714, 2005.

Garel, F., Kaminski, E., Tait, S., Limare, A., A fluid dynamics perspective on the interpretation of the surface thermal signal of lava flows, in: Harris, A.J.L., De Groeve, T., Garel F., Carn, S.A. (eds), Detecting, modelling and responding to effusive eruptions. Geological Society, London, Special Publications, 426, 243-256, doi: 10.1144/SP426.6, 2015.

Garel, F., Kaminski, E., Tait, S., Limare, A., An analogue study of the influence of solidification on the advance and surface thermal signature of lava flows, Earth Planet. Sci. Lett., 396, 46-55, 2014.

Garel, F., Kaminski, E., Tait, S., Limare, A., An experimental study of the surface thermal signature of hot subaerial isoviscous gravity currents: Implications for thermal monitoring of lava flows and domes, J. Geophys. Res., 117:B02205, doi: 10.1029/2011JB008698, 2012.

Gordeev, E.I., Muravev, Ya D., Samoilenko, S.B., Volynets, A.O., Melnikov, D.V., Dvigalo, V.N, The Tolbachik fissure eruption of 2012–2013: Preliminary results, in Doklady Earth Sciences, 452, 2, 1046-1050, Springer US, 2013.

Guest, J.E., Kilburn, C.R.L., Pinkerton, H., Duncan, A.M., The evolution of lava flow-fields: observations of the 1981 and 1983 eruptions of Mount Etna, Sicily, Bull. Volcanol., 49, 527–540, 1987.

Harris A.J.L., Thermal Remote Sensing of Active Volcanoes. Cambridge, 2013.

Harris, A.J.L., De Groeve, T., Carn, S., Garel., F., Risk evaluation, detection and simulation during effusive eruption disasters, in: Harris, A.J.L., De Groeve, T., Garel F., Carn, S.A. (eds), Detecting, modelling and responding to effusive eruptions. Geological Society, London, Special Publications, 426, 1-22. doi:10.1144/SP426.11, 2016.

Harris, A.J. and Rowland, S.K., FLOWGO 2012: An updated framework for thermo-rheological simulations of channel-contained lava, In: Hawaiian Volcanoes: From Source to Surface, Geophysical Monograph Series, 208, 457-481, 2015.

Harris, A.J.L., Baloga, S., Lava discharge rates from satellite-measured heat flux, Geophys. Re. Lett., 36, L19302, doi:10.1029/2009GL039717, 2009.

Harris, A.J.L., Rowland, SK, Effusion rate controls on lava flow length and the role of heat loss: A review, from: Thordarson, T., Self, S., Larsen, G., Rowland, S.K., Hoskuldsson, A. (eds), 2009.

Harris, A.J.L., Dehn, J., Calvari, S., Lava effusion rate definition and measurement: A review, Bull. Volcanol., 70, 1-22, doi:10.100 7/s00445-007-0120-y, 2007a.

1030 Harris, A., Favalli, M., Mazzarini, F., Pareschi, M.T., Best-fit results from application of a thermo-
1031 rheological model for channelized lava flow to high spatial resolution morphological data,
1032 Geophys. Res. Lett., 34(L01301), doi:10.1029/2006GL028126, 2007b.

1033 Harris, A., Favalli, M., Mazzarini, F., Pareschi, M., Best-fit results from application of a thermo-
1034 rheological model for channelized lava flow to high spatial resolution morphological data,
1035 Geophys. Res. Lett., 34, L01301, 2007.

1036 Harris, A., Dehn, J., Patrick, M., Calvari, S., Ripepe, M., Lodato, L., Lava effusion rates from
1037 hand-held thermal infrared imagery: An example from the June 2003 effusive activity at
1038 Stromboli, Bull. Volcanol., 68, 107-117, 2005.

1039 Harris, A.J.L. and Rowland, S., FLOWGO: A kinematic thermo-rheological model for lava flowing
1040 in a channel, Bull. Volc., 63, 20-44, 2001.

1041 Harris, A.J.L., Flynn, L.P., Keszthelyi, L., Mouginis-Mark, P.J., Rowland, S.K., Resing, J.A.,
1042 Calculation of lava effusion rates from Landsat TM data, Bull. Volcanol., 60, 52-71, 1998.

1043 Harris, A.J.L., De Groeve, T., Garel, F., Carn, S.A.,, Detecting, Modelling and Responding to
1044 Effusive Eruptions, Geological Society, London, Special Publications, 426,
1045 doi.org/10.1144/SP426.29, 2016.

1046 Hearn, D.R., Digenis, C.J., Lencioni, D.E., Mendenhall, J.A., Evans, J.B., Welsh, R.D., EO-1
1047 Advanced Land Imager overview and spatial performance, in Geosci. Rem. Sens. Symp.,
1048 2001, IGARSS'01, IEEE 2001 International, vol. 2, 897-900, 2001.

1049 Holman, J.P., Heat Transfer, 2nd ed., London: McGraw Hill, 713 p., 1992.

1050 Hon, K., Kauahikaua, J., Denlinger, R. and McKay, K., Emplacement and inflation of pahoehoe
1051 sheet flows: observations and measurements of active lava flows on Kilauea volcano, Hawaii,
1052 Geol. Soc. Am. Bull., 106, 351-370, 1994.

1053 Hawaii Volcano Observatory (HVO), Kīlauea Volcano – 2018 Summit and Lower East Rift Zone
1054 (LERZ) Brief Overview of Events April 17 to October 5, 2018, HVO Report, 2018.

1055 Kahle, A.B., Adams, M.J., Abbott, E.A., Mouginis-Mark, P.J. Realmuto, V.J., Remote Sensing
1056 on Mauna Loa, Am. Geophys. Un. Monogr., 92, 145-170, 1995.

1057 Kamchatka Volcanic Eruption Response Team (KVERT), Plosky Tolbachik, VONA/KVERT
1058 Weekly Release, http://www.kscnet.ru/ivs/kvert/van/index.php?type=3m, December 06,
1059 23:02 UTC, 2012.

1060 Kilburn, C.R.J., Lava crusts, a'a flow lengthening and the pahoehoe-a'a transition, Active Lavas:
1061 Monitoring and Modelling, 263-280, 1993.

1062 Kubanek, J., Richardson, J.A., Charbonnier, S.J., Connor, L.J., Lava flow mapping and volume
1063 calculations for the 2012–2013 Tolbachik, Kamchatka, fissure eruption using bistatic
1064 TanDEM-X InSAR, Bull. Volcanol., 77(12), 106, 2015.

1065 Lee, R.J. and Ramsey, M.S., What is the emissivity of active basaltic lava flows?, AGU Fall Mtg.,
1066 2016.

1067 Lee, R.J., King, P.L. and Ramsey, M.S., Spectral analysis of synthetic quartzofeldspathic
1068 glasses using laboratory thermal infrared spectroscopic methods, J. Geophys. Res., 115,
1069 B06202, doi:10.1029/2009JB006672, 2010.

1070 Lillesand, T.M. and Kiefer, R.W. Remote Sensing and Image Interpretation, New York: John
1071 Wiley & Sons, 721 p., 1987.

1072 Melnikov, D. and Volynets, A.O., Remote sensing and petrological observations on the 2012–
1073 2013 fissure eruption at Tolbachik volcano, Kamchatka: Implications for reconstruction of the
1074 eruption chronology, J. Volcanol. Geotherm. Res., 307, 89-97, 2015.

1075 Miyamoto, H. and Papp, K. Rheology and topography control the path of a lava flow: Insight from
1076 numerical simulations over a preexisting topography, Geophys. Res. Lett., 31, L16608,
1077 doi:10.1029/2004GL020626, 2004.

1078 Miyamoto, H., Sasaki, S., Simulating lava flows by an improved cellular automata method,
1079 Comp. Geosci., 23 (3), 283-291, 1997.

1080 Miyamoto, H., Crown, D.A., A simplified two-component model for the lateral growth of pahoehoe
1081 lobes, J. Volcanol. Geotherm. Res., 157 (4), 331-342, 2006.

1082 MODVOLC website, http://modis.higp.hawaii.edu/, 2013.

1083 Moxham, R.M., Thermal surveillance of volcanoes, In The surveillance and prediction of volcanic
1084 activity, Paris, Unesco, p. 103-124, 1971.

1085 Neal, C.A., et al., The 2018 rift eruption and summit collapse of Kīlauea Volcano, Science,
1086 10.1126/science.aav7046, 2018.

1087 Peterson, D.W., Holcomb, R.T., Tilling, R.I., Christiansen, R.L., Development of lava tubes in
1088 the light of observations at Mauna Ulu, Kilauea volcano, Hawaii, Bull. Volcanol., 56, 343e360,
1089 1994.

1090 Pieri, D.C., Glaze, L.S., Abrams, M.J., Thermal radiance observations of an active lava flow
1091 during the June 1984 eruption of Mount Etna, Geology, 18, 1018-1022, 1990.

1092 Pieri, D., Baloga, S.M., Eruption rate, area, and length relationships for some Hawaiian lava
1093 flows, J. Volcanol. Geotherm. Res., 30, 29-45, 1986.

1094 Plechov, P., Blundy, J., Nekrylov, N., Melekhova, E., Shcherbakov, V., Tikhonova, M.S.,
1095 Petrology and volatile content of magmas erupted from Tolbachik Volcano, Kamchatka,
1096 2012–13, J. Volcanol. and Geotherm. Res., 307, 182-199, 2015.

1097 Ramsey, M.S. and Fink, J.H., Estimating silicic lava vesicularity with thermal remote sensing: A
1098 new technique for volcanic mapping and monitoring, Bull. Volcanol., 61, 32-39, 1999.

1099 Ramsey, M.S., Chevrel, M.O., Harris, A.J.L., Modeling the 2012-2013 lava flows of Tolbachik,
1100 Russia using thermal infrared satellite data and PyFLOWGO, AGU Fall Mtg., 2017.

1101 Ramsey, M.S., Synergistic use of satellite thermal detection and science: A decadal perspective
1102 using ASTER, in: Harris, A.J.L., De Groeve, T., Garel, F. and Carn, S.A. (eds.), Detecting,
1103 Modelling and Responding to Effusive Eruptions, Geol. Soc., London, Special Publications,
1104 426, doi:10.1144/SP426.23, 115-136, 2016.

Ramsey, M.S. and Harris, A.J.L., Modelling the thermal and infrared spectral properties of active vents: Comparing basaltic lava flows of Tolbachik, Russia to Arsia Mons, Mars, AGU Fall Mtg., 2016.

Ramsey. M.S. and Harris, A.J.L., Volcanology 2020: How will thermal remote sensing of volcanic surface activity evolve over the next decade?, J. Volcanol. Geotherm. Res., 249, 217-233, 2013.

Ramsey, M.S., Wessels, R.L., Anderson, S.W., Surface textures and dynamics of the 2005 lava dome at Shiveluch Volcano, Kamchatka, Geol. Soc. Amer. Bull., doi:10.1130/B30580.1, 2012.

Ramsey, M.S. and Dehn, J., Spaceborne observations of the 2000 Bezymianny, Kamchatka eruption: The integration of high-resolution ASTER data into near real-time monitoring using AVHRR, J. Volc. Geotherm. Res., 135, 127-146, 2004.

Rhéty, M., Harris, A., Villeneuve, N., Gurioli, L., Médard, E., Chevrel, O. and Bachélery, P., A comparison of cooling-limited and volume-limited flow systems: Examples from channels in the Piton de la Fournaise April 2007 lava-flow field, Geochem., Geophys., Geosyst., 18(9), 3270-3291, 2017.

Riker, J.M., Cashman, K.V., Kauahikaua, J.P., Montierth, C.M., The length of channelized lava flows: Insight from the 1859 eruption of Mauna Loa Volcano, Hawaii. J. Volcanol. Geotherm. Res. 183, 139-156, 2009.

Robert, B., Harris, A., Gurioli, L., Médard, E., Sehlke, A., Whittington, A., Textural and rheological evolution of basalt flowing down a lava channel, Bull. Volcanol., 76, 824, doi: 10.1007/s00445-014-0824-8, 2014.

Rose, S.R., Watson, I.M., Ramsey, M.S., Hughes, C.G., Thermal deconvolution: Accurate retrieval of multispectral infrared emissivity from thermally-mixed volcanic surfaces, Rem. Sens. Environ., 140, 690-703, 2014.

Rose, S.R. and Ramsey, M.S., The 2005 eruption of Kliuchevskoi volcano: Chronology and processes derived from ASTER spaceborne and field-based data, J. Volc. Geotherm. Res., 184, 367–380, 2009.

Rothery, D.A., Francis, P.W., Wood, C.A., Volcano monitoring using short wavelength infrared data from satellites, J. Geophys. Res., 93(B7), 7993-8008, 1988.

Sawyer, G.M. and Burton, M.R., Effects of a volcanic plume on thermal imaging data, Geophys. Res. Lett., 33, L14311. DOI: 10.1029/2005GL025320, 2006.

Tachikawa, T., Hato, M., Kaku, M. and Iwasaki, A., Characteristics of ASTER GDEM version 2, Geosci. Rem. Sens. (IGARSS), 2011 IEEE International, 3657-3660, 2011.

Tarquini, S., A review of mass and energy flow through a lava flow system: Insights provided from a non-equilibrium perspective, Bull. Volcanol., 79, 64, doi:10.1007/s00445-017-1145-5, 2017.

van Rossum, G., Python tutorial, Technical Report CS-R9526, Centrum voor Wiskunde en Informatica (CWI), Amsterdam, May 1995.

1144 Volynets, A.O., Edwards, B.R., Melnikov, D., Yakushev, A., Griboedova, I., Monitoring of the
1145 volcanic rock compositions during the 2012-2013 fissure eruption at Tolbachik volcano,
1146 Kamchatka, J. Volcanol. Geotherm. Res., 307, 120-132, 2015.

1147 Walker, G.P.L., Lengths of Lava Flows, Philos. Trans. Roy. Soc. Lond., 274, 107-118, 1973.

1148 Walker, G.P.L., Basaltic volcanoes and volcanic systems. In: Sigurdsson, H. (ed.), Encyclopedia
1149 of Volcanoes, Academic Press, 283-289, 2000.

1150 Wessels, R.L., Ramsey, M.S., Dehn, J., Senyukov, S., Mapping elevated temperatures on a
1151 thirty-year-old basalt flow of New Tolbachik Volcano using satellite and ground-based
1152 thermal infrared, Eos Trans. AGU, 86(52): Fall Mtg. Suppl., abs. V31A-0605, 2005.

1153 Wooster, M.J., Zhukov, B., Oertel, D., Fire radiative energy for quantitative study of biomass
1154 burning: Derivation from the BIRD experimental satellite and comparison to MODIS fire
1155 products, Rem. Sens. Environ., 86, 83-107, doi:10.1016/S0034-4257(03)00070-1, 2003.

1156 Wright, R., Garbeil, H., Harris, A.J., Using infrared satellite data to drive a thermo-
1157 rheological/stochastic lava flow emplacement model: A method for near-real-time volcanic
1158 hazard assessment, Geophys. Res. Lett., 35, 1-5, 2008.

1159 Wright, R., Flynn, L.P., Garbeil, H., Harris, A.J.L., Pilger, E., Automated volcanic eruption
1160 detection using MODIS, Rem. Sens. Environ., 82, 135-155, 2002.

1161 Wright, R., Blake, S., Harris, A., Rothery, D., A simple explanation for the space-based
1162 calculation of lava eruptions rates, Earth Planet. Sci. Lett., 192, 223-233, doi:10.1016/S0012-
1163 821X(01)00443-5, 2001.

1164 Wright, R. and Flynn, L.P., On the retrieval of lava-flow surface temperatures from infrared
1165 satellite data, Geology, 31(10), 893-896, 2003.

1166 Yamaguchi, Y., Kahle, A.B., Tsu, H., Kawakami, T. and Pniel, M., Overview of Advanced
1167 Spaceborne Thermal Emission and Reflection Radiometer (ASTER), IEEE Trans. Geosci.
1168 Rem. Sens., 36, doi:10.1109/36.700991, 1062-1071, 1998.